4th Dec

Kramer, D. M., Johnson, G., Kiirats, O., & Edwards, G. E. (2004). New fluorescence parameters for the determination of QA redox state and excitation energy fluxes. *Photosynthesis research*, *79*(2), 209-218.

$$\phi_{NO} = \frac{1}{NPQ + 1 + q_L(F_M/F_O - 1)}. \qquad (51)$$

From this we can calculate ϕ_{NPQ}, as:

$$\phi_{NPQ} = 1 - \phi_{II} - \frac{1}{NPQ + 1 + q_L(F_M/F_O - 1)}. \qquad (52)$$

How to estimate quantum yield of Fluorescence

3rd Dec

Liu, Z., Zhao, F., Liu, X., Yu, Q., Wang, Y., Peng, X., ... & Lu, X. (2022). Direct estimation of photosynthetic CO2 assimilation from solar-induced chlorophyll fluorescence (SIF). *Remote Sensing of Environment*, *271*, 112893.

were set to F_o and F_m measured by PAM fluorometry, respectively. Our results showed that K_{DF} varied in a small range between 11.0 and 12.7 (Table 1). Note that Φ_{Fmax} should increase as PAR_{SP} increases. Thus, K_{DF} decreases with increased PAR_{SP} and reaches its minimum value at infinite PAR_{SP}. In other words, K_{DF} should at least be smaller than 11.0. We therefore assumed $K_{DF} = 9$ in this study ($K_D = 0.9$ and $K_F = 0.1$).

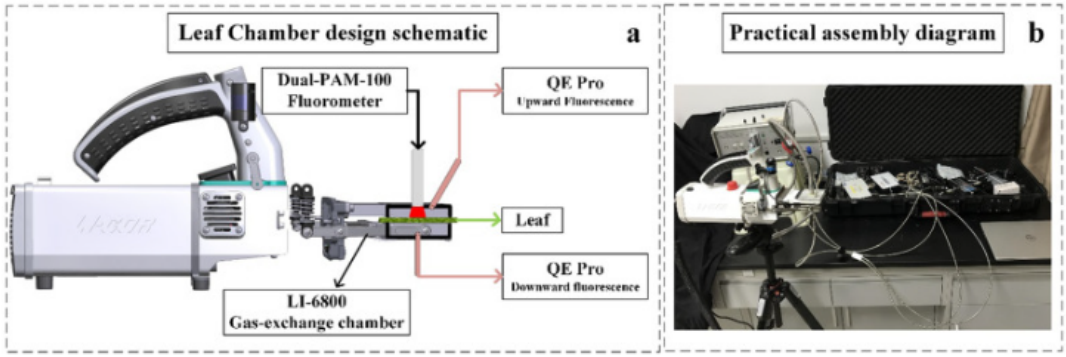

Download : Download high-res image (266KB) Download : Download full-size image

Fig. 3. Schematic of the K_{DF} measurement system. (a) a customized leaf chamber coupled with a pulse-amplitude modulation (PAM) fluorometer and two spectrometers to conduct fluorescence flux measurements induced by a saturation pulse in dark-adapted conditions. The black rectangle indicates that the leaf chamber was painted with black acrylic paint as a light trap, and the red trapezoid represents a saturation light pulse emitting from a PAM fluorometer. (b) a photograph of the K_{DF} measurement system including an LI-6800 gas-exchange chamber (LI-COR Biosciences, Lincoln, Nebraska, USA), a Dual-PAM-100 fluorometer (Dual-PAM-100, Heinz Walz GmbH, Effeltrich, Germany), and two QE Pro spectrometers (Ocean Optics, Dunedin, Florida, USA). (For interpretation of the references to colour in this figure legend, the reader is referred to the web version of this article.)

How to estimate quantum yield of Fluorescence

2nd Dec

Zhang, C., Atherton, J., Peñuelas, J., Filella, I., Kolari, P., Aalto, J., ... & Porcar-Castell, A. (2019). Do all chlorophyll fluorescence emission wavelengths capture the spring recovery of photosynthesis in boreal evergreen foliage?. *Plant, cell & environment*, *42*(12), 3264-3279.

2.3 Continuous measurements of PAM ChlF *in situ*

A Monitoring PAM system (MONI-PAM, Walz GmbH, and Germany; Porcar-Castell, 2011; Porcar-Castell, Pfündel, Korhonen, & Juurola, 2008), equipped with four independent PAM fluorometers, was used to record the instantaneous fluorescence yield (F), the maximal fluorescence yield (F'_M), incoming PAR, and temperature every 30 min. Night F and F_M were assumed to correspond to minimal (F_o) and maximal (F_M) fluorescence and used to derive daily maximum quantum yield of PSII, F_V/F_M after Kitajima and Butler (1975), and to calculate quenching parameters NPQ_S and PQ_S after Porcar-Castell (2011) as follows: $NPQ_S = F_{MR}/F_M - 1$ and $PQ_S = F_{MR}/F_o - F_{MR}/F_M$, where F_{MR} is the summer night reference obtained for those particular needles in the absence of NPQ_S. A decrease in PQ_S relative to summer levels was here interpreted in terms of photoinhibition of reaction centres (Porcar-Castell, 2011). Finally, seasonal changes in PAM based fluorescence yield (Φ_F) were estimated as $\Phi_F = 0.1\ F_o/F_{MR}$ (Porcar-Castell, 2011, note the unfortunate typo in equation 24 therein where F'_M should be F_{MR}), which is based on the assumption of a maximum fluorescence yield of 10% for PSII particles at the F_M state (Barber, Malkin, & Telfer, 1989). The four fluorometers were installed in top canopy branches pointing south.

How to estimate quantum yield of Fluorescence

1st Dec

Wu, G., Guan, K., Jiang, C., Kimm, H., Miao, G., Bernacchi, C. J., ... & Chen, M. (2022). Attributing differences of solar-induced chlorophyll fluorescence (SIF)-gross primary production (GPP) relationships between two C4 crops: corn and miscanthus. *Agricultural and Forest Meteorology*, *323*, 109046.

For both LI-6800 and Moni-PAM measurements, leaf-level $\Phi_{F,\,Leaf}$, Φ_P, quantum yield of heat dissipation through NPQ (Φ_N), and quantum yield of constitutive heat dissipation (Φ_D) were estimated. $\Phi_{F,\,Leaf}$ was calculated based on expression proposed by Gu et al. (2019a):

$$\Phi_{F,\,Leaf} = \frac{1-\phi_{P,\,max}}{(1+K_{DF})[(1+NPQ)\times(1-\Phi_{P,max})+q_L\times\,\Phi_{P,max}]} \quad (7)$$

$$\Phi_{P,max} = 1 - \frac{F_0}{F_M}$$

$$NPQ = \frac{F_M}{F_{M'}} - 1$$

$$q_L = \frac{F'_M - F_S}{F'_M - F'_0} \times \frac{F'_0}{F_S}$$

where $\Phi_{P,\,max}$ is the maximum photochemical yield calculated from the dark-adapted minimum and maximum fluorescence; NPQ quantifies the non-photochemical quenching heat dissipation process; q_L represents the fraction of photosystem II reaction centers with fully oxidized primary quinone electron acceptor; K_{DF} is the ratio of rate constant of constitutive heat dissipation (K_D) to rate constant of fluorescence emission (K_F), and assumed to be constant 19 (Gu et al., 2019a). Φ_P was calculated based on expression proposed by Genty et al. (1989):

How to estimate quantum yield of Fluorescence

4th Nov

Shi, S., Cong, W., Lu, S., Zhao, T., Wang, F., & Lu, Q. (2022). Can SIF and NPQ be used in the photosynthesis rate simulation of plants subjected to drought?. *Environmental and Experimental Botany*, *203*, 105067.

where F_O' is the minimum ChlF measured by the far-red light to obtain the maximal oxidation of the PQ pool (Kramer et al., 2004), which could be calculated as (Genty et al., 1989, Kramer et al., 2004):

$$F_o' = \frac{F_o}{\Phi_{\mathrm{PSII\ max}} + \frac{F_o}{F_m'}}. \quad (3)$$

The leaf level SIF of the *L. chinensis* was calculated from the theoretical equation (Gu et al., 2019, Porcar-Castell et al., 2014):

$$SIF = \frac{1-\Phi_{\mathrm{PS\ II\ max}}}{(1+k_{DF})\times[(1+NPQ)\times(1-\Phi_{\mathrm{PS\ II\ max}})+qL\times\Phi_{\mathrm{PS\ II\ max}}]} \times PAR \times \alpha \times \beta, \quad (4)$$

where PAR is the light intensity (μmol PPFD m^{-2} s^{-1}); α is the leaf absorptance (0.84, Björkman and Demmig, 1987; Schreiber, 2004); β is the fraction of light allocated to PSII (0.5, von Caemmerer, 2000); and k_{DF} is k_D/k_F, with k_D and k_F representing the rate constants of constitutive thermal dissipation and fluorescence, respectively, assuming that k_{DF} is 10 (Pfündel, 1998).

How to estimate quantum yield of Fluorescence

3rd Nov

Joshi, J., Stocker, B. D., Hofhansl, F., Zhou, S., Dieckmann, U., & Prentice, I. C. (2022). Towards a unified theory of plant photosynthesis and hydraulics. *Nature Plants*, *8*(11), 1304-1316.

Fig. 1: Schematic representation of our model, underlying first principles and notation.

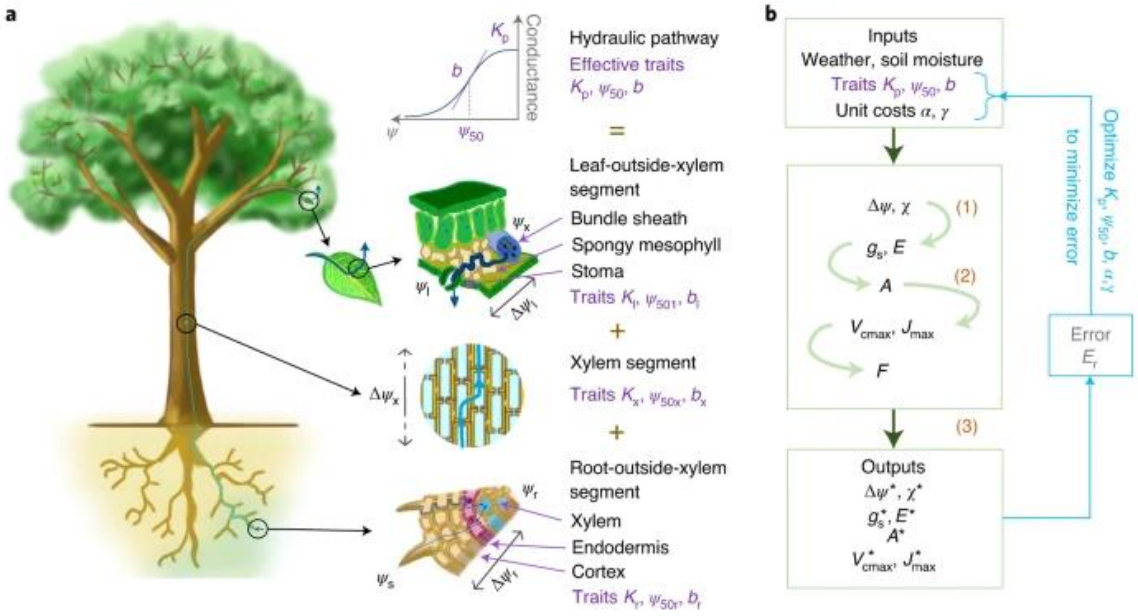

Model about photosynthesis and hydraulics

2nd Nov

Zhao, M., Liu, Y., & Konings, A. G. (2022). Evapotranspiration frequently increases during droughts. *Nature Climate Change*, *12*(11), 1024-1030.

Fig. 1: $P(\mathrm{ET}^{+}_{\mathrm{drought}})$ comparison between our observations and CMIP6 ESM simulations.

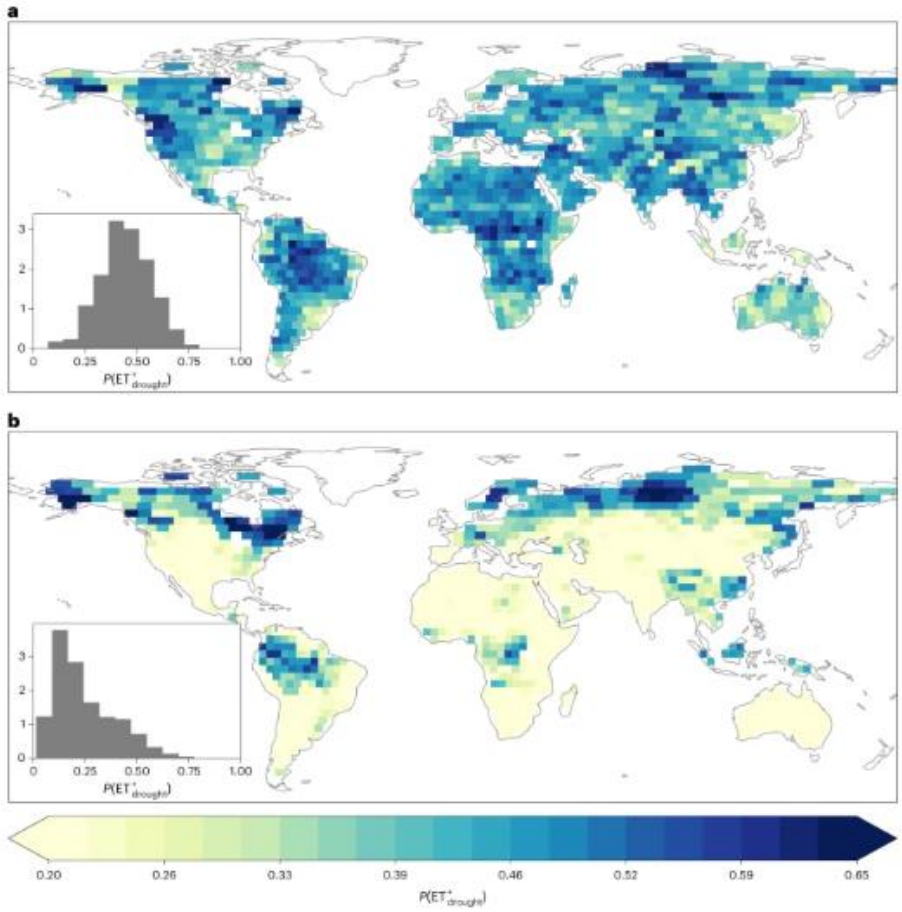

a, Observed $P(\mathrm{ET}^{+}_{\mathrm{drought}})$ during droughts between 2003 and 2020. **b**, $P(\mathrm{ET}^{+}_{\mathrm{drought}})$ based on the CMIP6 ESM ensemble mean. The insets in **a** and **b** show the probability density function (PDF) of each location's $P(\mathrm{ET}^{+}_{\mathrm{drought}})$ across the globe. Basemap from Natural Earth (https://www.naturalearthdata.com/).

Full size image >

What about ET under drought stress condition?

1st Nov

Boucher, P. B., Paynter, I., Orwig, D. A., Valencius, I., & Schaaf, C. (2021). Sampling forests with terrestrial laser scanning. *Annals of Botany*, *128*(6), 689-708.

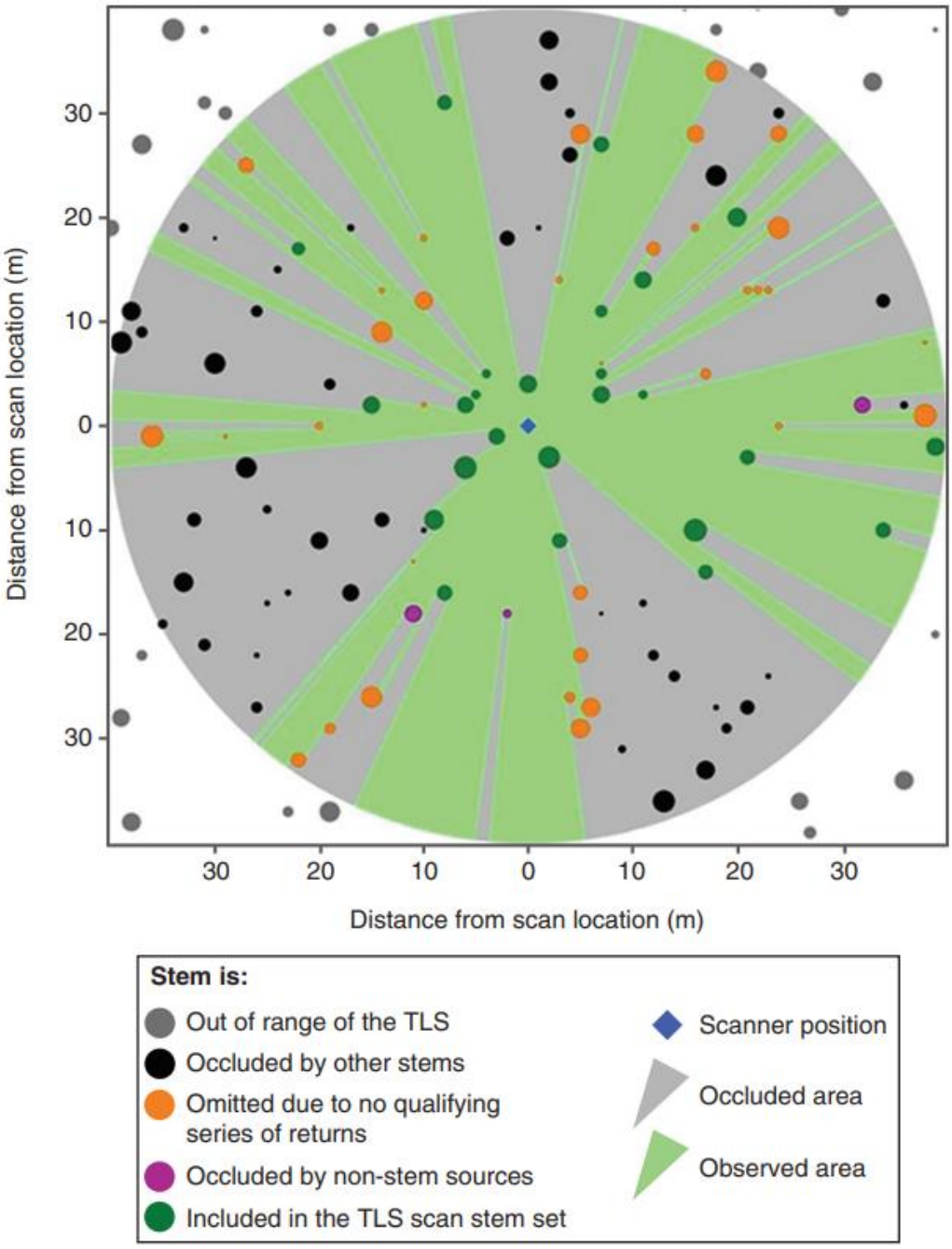

What is the TLS footprint in Forest?

4th Oct

Disney, M. (2021). How can we know what we don't know? A Commentary on: Sampling forests with terrestrial laser scanning. *Annals of Botany*.

Fig. 1.

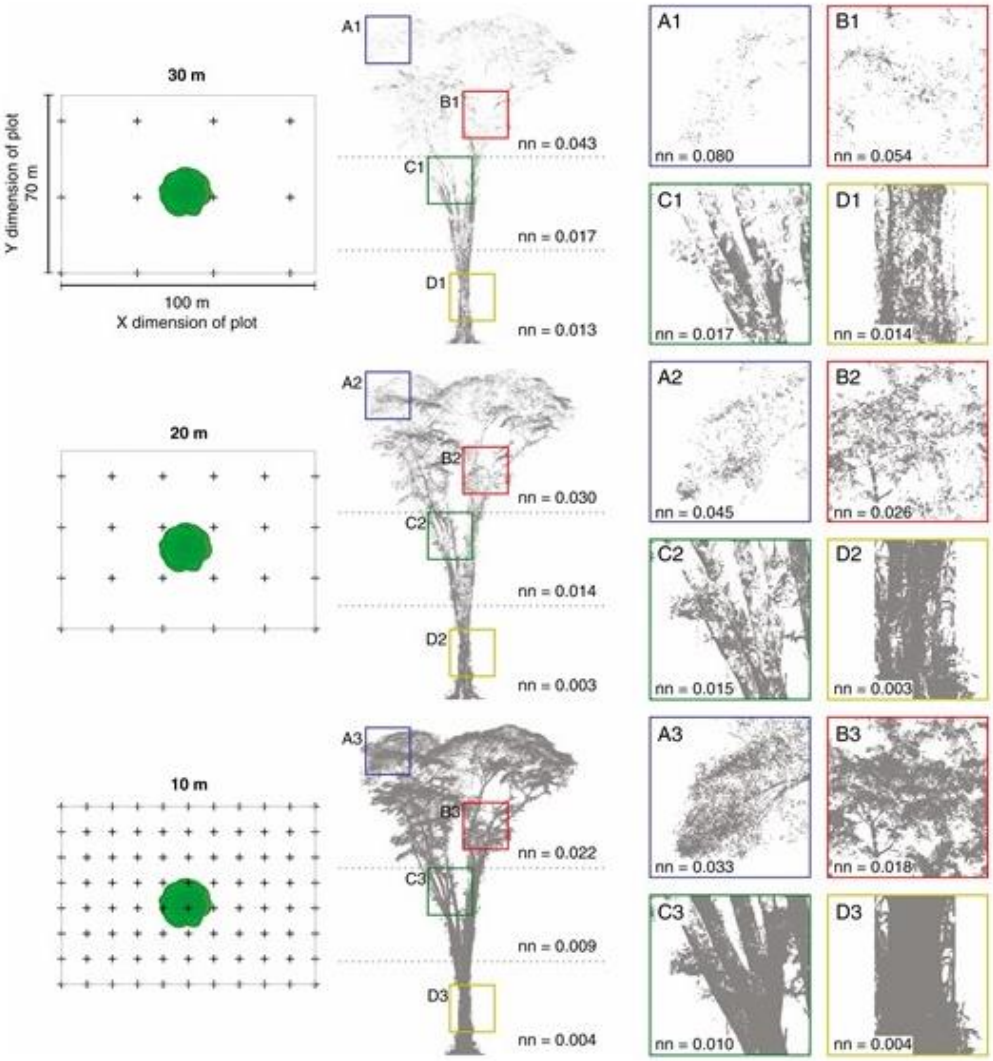

What is the TLS sampling interval in Forest?

3rd Oct

Bittner, T., Irrgang, K. D., Renger, G., & Wasielewski, M. R. (1994). Ultrafast excitation energy transfer and exciton-exciton annihilation processes in isolated light harvesting complexes of photosystem II (LHC II) from spinach. *The Journal of Physical Chemistry*, *98*(46), 11821-11826.

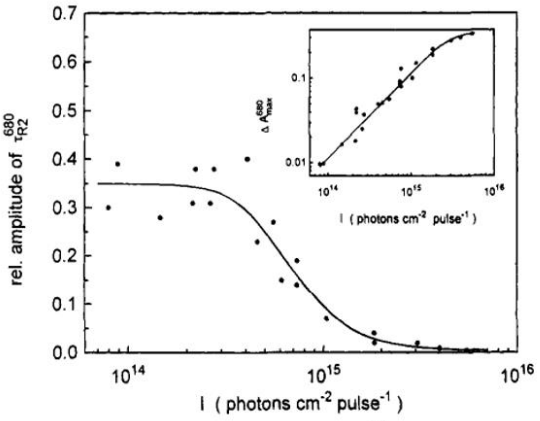

Figure 5. Relative amplitude of the lifetime τ_{R2}^{680} in isolated LHC II complexes as a function of the excitation intensity. Inset: maximum amplitude of the fitted transient absorption changes at 680 nm in dependence on the excitation intensity.

From the new structural data on LHC II it was proposed that all Chl *b* molecules can transfer their excitation energy to Chl *a* molecules with high efficiency.[3] Each of the tetrapyrrole rings assigned to Chl *b* is in close contact with another ring that is assumed to represent a Chl *a* molecule. The center-to-center distances are in all cases between 8 and 10 Å. Theoretical calculations within the framework of Förster theory give a transfer time of about 1 ps for a distance of 10 Å between Chl *b* and Chl *a*.[14] However, the application of Förster theory to

WHY Chlorophyll “a” fluorescence?

2nd Oct

Williams, D. L. (1991). A comparison of spectral reflectance properties at the needle, branch, and canopy level for selected conifer species. *Remote Sensing of Environment*, *35*(2-3), 79-93.

Figure 6. Branch-level mean spectral reflectance characteristics for Norway spruce, red pine, white pine, and sugar maple when nearly equal LAI values (≈ 5.5) were within the FOV of the spectrometer. (See Table 1 for LAI, number of branches needed to attain that LAI, and standard deviation information.)

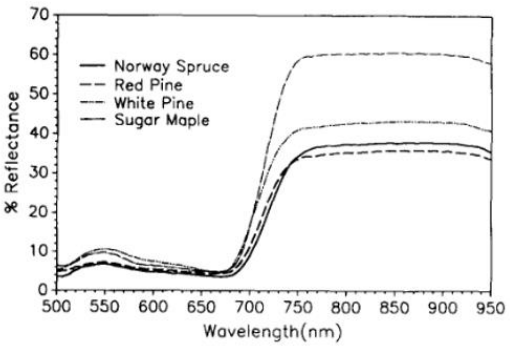

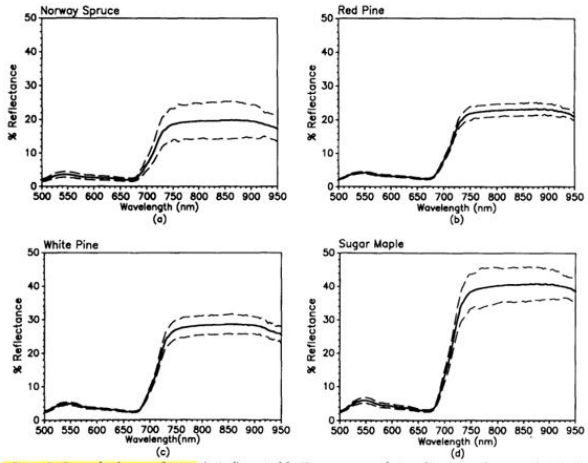

Figure 7. Canopy-level mean reflectance (±1 sd) acquired for Norway spruce, red pine, white pine, and sugar maple/mixed hardwood stands using the helicopter-borne data acquisition system.

WHY ENF leaf and canopy reflectance is lower than others?

1st Oct

Preisler, Y., Grünzweig, J., Ahiman, O., Oz, I., Feng, X., Muller, J., ... & Yakir, D. (2022). Vapor pressure deficit is not a limiting factor for gas exchange in a mature dryland forest.

Vapor pressure deficit is not a limiting factor for gas exchange in a mature dryland forest

DROUGHT | SUPPLY AND DEMAND | TRANSPIRATION | VPD | WATER RELATIONS

Yakir Preisler, José Grünzweig, Ori Ahiman, Itay Oz, Xue Feng, Jonathan Muller, Madi Amer, Nadine Ruehr, Eyal Rotenberg, Benjamin Birami, Dan Yakir

Abstract

Climate change is often associated with increasing vapor pressure deficit (VPD) and decreasing soil moisture (SM). While atmospheric and soil drying often co-occurs, their differential effects on plant functioning and productivity remain uncertain. We aimed to elaborate on the divergent effects and underlying mechanisms of soil and atmospheric drought, based on continuous, in situ measurements of branch gas exchange, with automated chambers, in a mature semiarid Aleppo pine forest. We investigated the response of control trees exposed to combined soil-atmosphere drought (low SM, high VPD) during the rainless Mediterranean summer, and that of trees experimentally unconstrained by soil dryness (high SM; using supplementary dry season water supply) but subjected to atmospheric drought (high VPD). During the seasonal dry period, branch conductance (g_{br}), the rates of transpiration (E) and net photosynthesis (A_{net}) decreased in low-SM trees but greatly increased in high-SM trees. The response of E and g_{br} to the massive rise in VPD (to a maximum of 7 kPa) was negative in low-SM trees and positive in high-SM trees. These observations were consistent with predictions based on a simple plant hydraulic model showing that plant water potential is a good predictor of the g_{br} and E response to VPD. These results demonstrate that the release from drought on the supply-side, in combination with plant hydraulic regulation, eliminates the effect of atmospheric demand (VPD) as a stressor and on canopy gas exchange in mature, drought-adapted pine trees.

4th Sep

Schönbeck, L. C., Schuler, P., Lehmann, M. M., Mas, E., Mekarni, L., Pivovaroff, A. L., ... & Grossiord, C. (2022). Increasing temperature and vapor pressure deficit lead to hydraulic damages in the absence of soil drought. *Plant, Cell & Environment*.

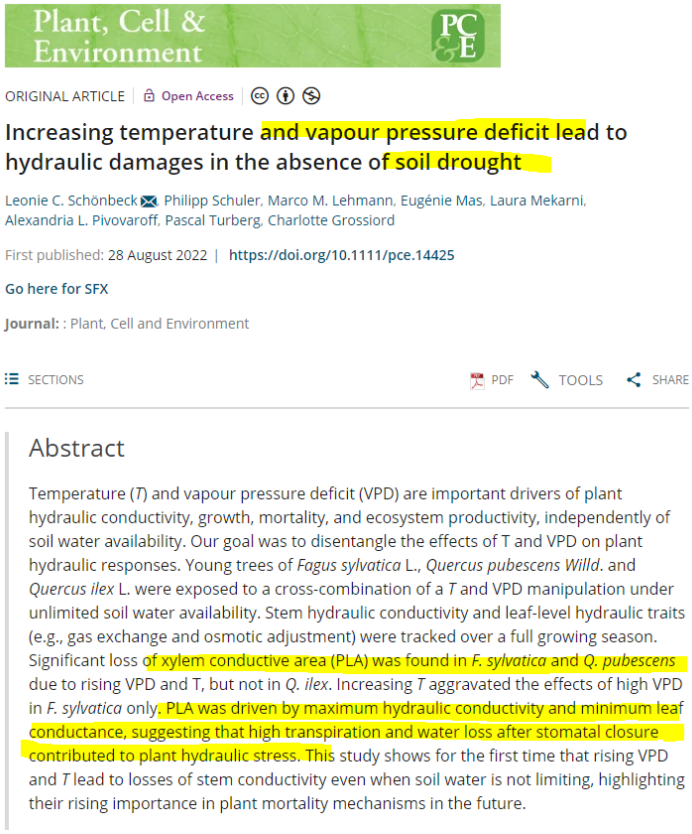

Plant, Cell & Environment

ORIGINAL ARTICLE | Open Access

Increasing temperature and vapour pressure deficit lead to hydraulic damages in the absence of soil drought

Leonie C. Schönbeck, Philipp Schuler, Marco M. Lehmann, Eugénie Mas, Laura Mekarni, Alexandria L. Pivovaroff, Pascal Turberg, Charlotte Grossiord

First published: 28 August 2022 | https://doi.org/10.1111/pce.14425

Go here for SFX

Journal: : Plant, Cell and Environment

SECTIONS PDF TOOLS SHARE

Abstract

Temperature (*T*) and vapour pressure deficit (VPD) are important drivers of plant hydraulic conductivity, growth, mortality, and ecosystem productivity, independently of soil water availability. Our goal was to disentangle the effects of T and VPD on plant hydraulic responses. Young trees of *Fagus sylvatica* L., *Quercus pubescens Willd*. and *Quercus ilex* L. were exposed to a cross-combination of a *T* and VPD manipulation under unlimited soil water availability. Stem hydraulic conductivity and leaf-level hydraulic traits (e.g., gas exchange and osmotic adjustment) were tracked over a full growing season. Significant loss of xylem conductive area (PLA) was found in *F. sylvatica* and *Q. pubescens* due to rising VPD and T, but not in *Q. ilex*. Increasing *T* aggravated the effects of high VPD in *F. sylvatica* only. PLA was driven by maximum hydraulic conductivity and minimum leaf conductance, suggesting that high transpiration and water loss after stomatal closure contributed to plant hydraulic stress. This study shows for the first time that rising VPD and *T* lead to losses of stem conductivity even when soil water is not limiting, highlighting their rising importance in plant mortality mechanisms in the future.

Findings: Significant hydraulic damage in F. sylvatica and signs of drought stress in Q. pubescens! Minimum leaf conductance (gmin) was strongly correlated to the loss of conductivity in the stem, suggesting that even after stomatal closure, residual water loss can be dangerous.

So: can air drought give a small tree drought stress, even when the roots have enough water? Answer: YES!

3rd Sep

Fu, Z., Ciais, P., Prentice, I. C., Gentine, P., Makowski, D., Bastos, A., ... & Hajima, T. (2022). Atmospheric dryness reduces photosynthesis along a large range of soil water deficits. *Nature communications*, *13*(1), 1-10.

Fig. 1: Response of gross primary production to soil water content and vapor pressure deficit.

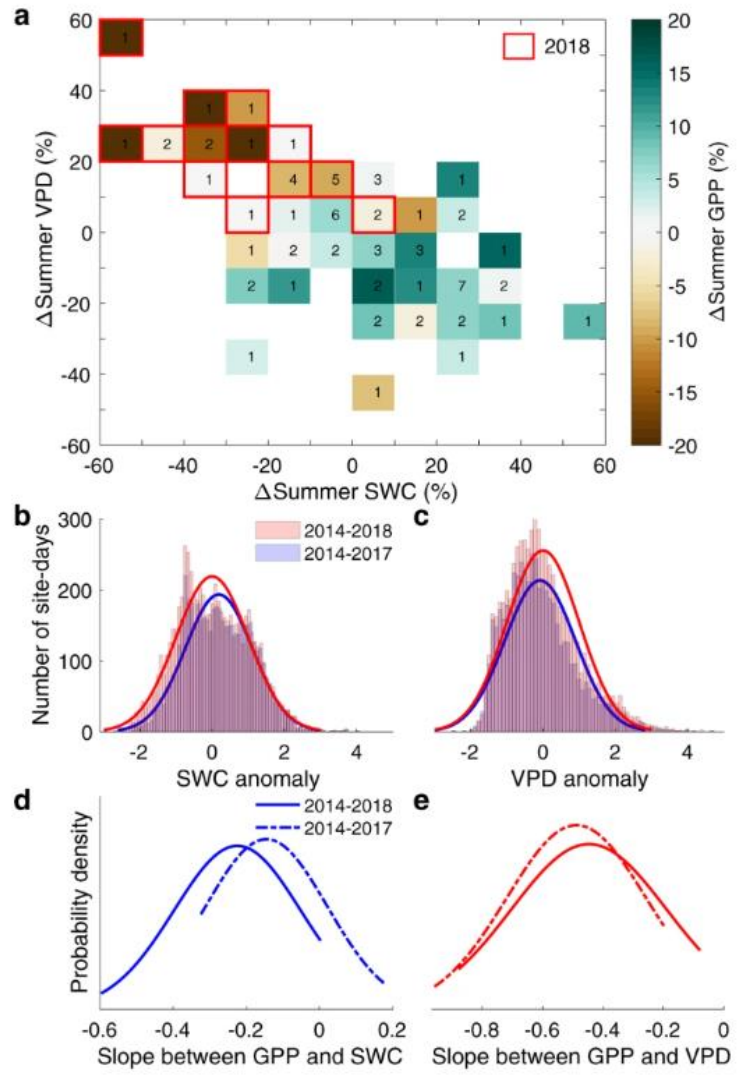

a The response of the relative changes of summer gross primary production (GPP) to the relative changes of summer soil water content (SWC) and vapor pressure deficit (VPD) during 2014–2018. The observations from 2018 are distributed in the highlighted boxes with red borders while the 2014–2017 are mainly distributed in the other boxes (see also Supplementary Fig. 1). The number indicates the number of sites in each bin. **b**–**c** Histogram with a distribution fit of the number of site-days for daily SWC (**b**) and VPD (**c**) anomalies during the summer across 2014–2018 and 2014–2017. **d**–**e** Probability distributions across all sites for the linear regression slope of daily GPP anomalies to SWC (**d**) and VPD anomalies (**e**) during the summer across 2014–2018 and 2014–2017. The negative sign for the slope

---

2nd Sep

Schumacher, D. L., Keune, J., Dirmeyer, P., & Miralles, D. G. (2022). Drought self-propagation in drylands due to land–atmosphere feedbacks. *Nature Geoscience*, *15*(4), 262-268.

Fig. 4: Upwind drought in drylands.

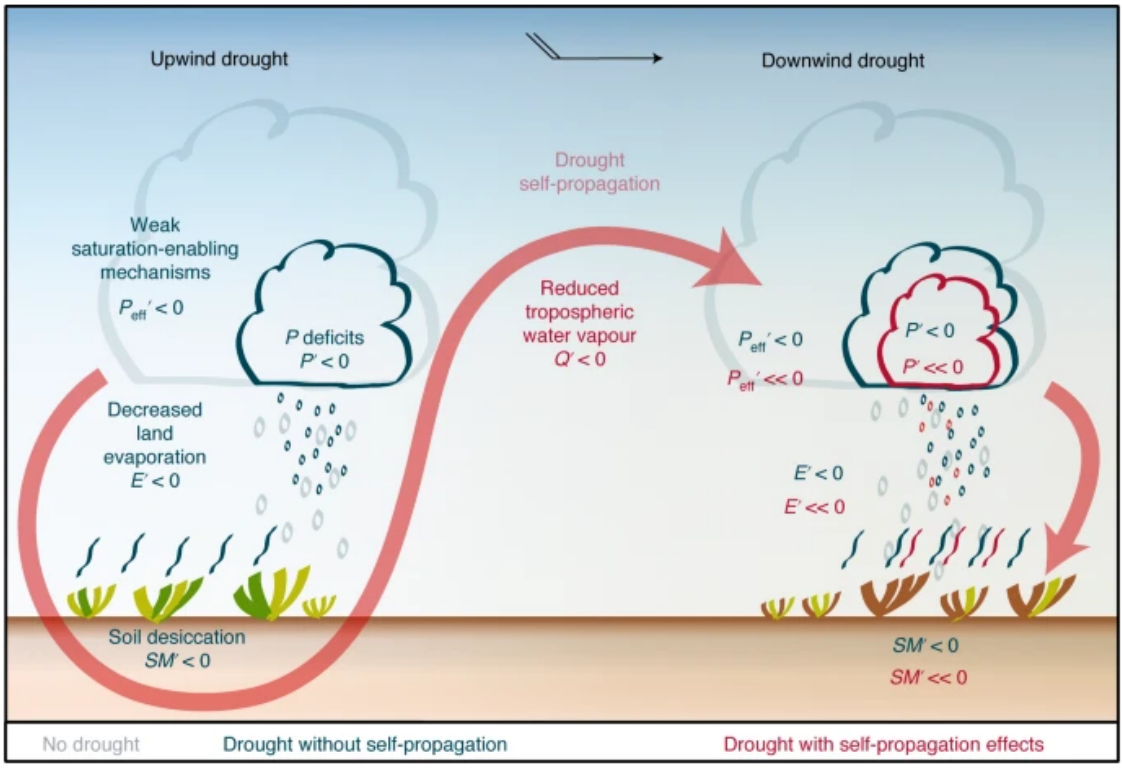

Meteorological drought is frequently triggered by weaker-than-usual dynamical saturation-enabling mechanisms (conceptualized as low precipitation efficiency; $P_{eff}' < 0$), which in turn may respond to a remote forcing, such as anomalous sea surface temperatures. Once that happens, limited precipitation ($P' < 0$) causes soil desiccation ($SM' < 0$) and soil stress, exacerbated by the high potential evaporation due to clear skies and elevated temperatures. Then, evaporation becomes (more) water limited ($E' < 0$). The reduction in near-surface air moistening—extending across the troposphere via vertical mixing—causes a reduction in water vapour being exported downwind ($Q' < 0$). Therefore, further downwind, for the same precipitation efficiency, even less precipitation is expected ($P' < 0$), contributing to downwind drought onset ($SM' < 0, E' < 0$). Moreover, since water vapour is known to enhance uplift, additional reductions are possible for convective precipitation ($P_{eff}', P', SM', E' \ll 0$).

1st Sep

Wang, B., Yue, X., Zhou, H., & Zhu, J. (2022). Impact of diffuse radiation on evapotranspiration and its coupling to carbon fluxes at global FLUXNET sites. *Agricultural and Forest Meteorology*, *322*, 109006.

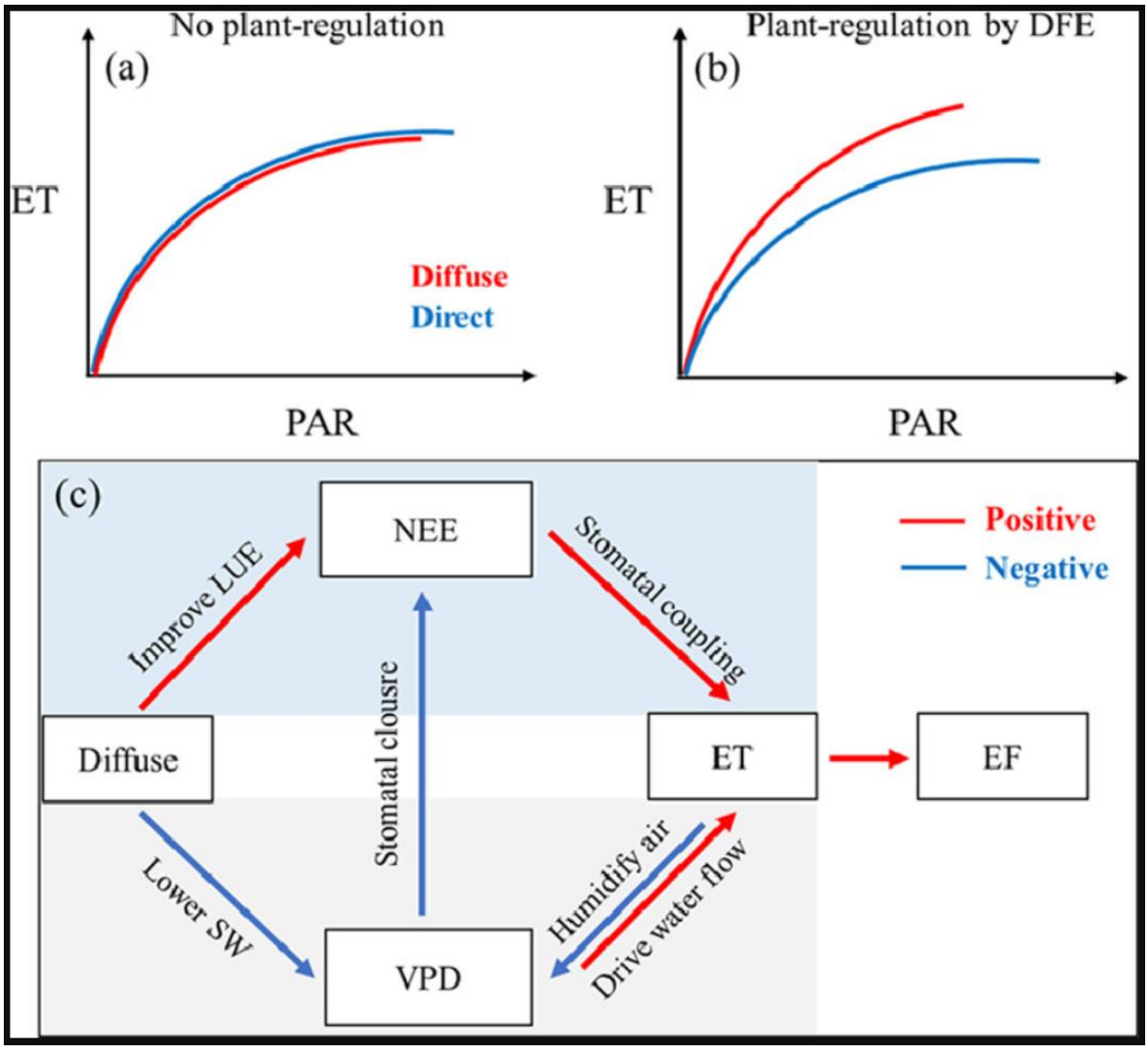

4th Aug

Ma, L., Yu, D., Zheng, G., Chen, Y., & Feng, K. (2022). Modeling the view-angle dependence of the gap fraction in subtropical forests by using terrestrial laser scanning. *Agricultural and Forest Meteorology*, *321*, 108976.

2.3.2. Estimating the directional gap fraction

Once the 3-D structure of forests from the TLS data is ready, the main factor determining the DGF is the view angle. Note that the view angle here is a parallel perspective because the incident solar beam or the view angle of the satellite is assumed to be parallel (Fig. 3). The DGF at a view angle of θ, φ and height h represents the fraction of viewed sky area within plot regions and is estimated as the ratio of gap area ($A_{gap\text{-}h}(\theta, \varphi)$) to plot area ($A_{all\text{-}h}(\theta, \varphi)$) (Fig. 3). Thus, the critical step is to calculate the projected areas of the gap and plot regions at different absolute or relative heights and view angles within a plot.

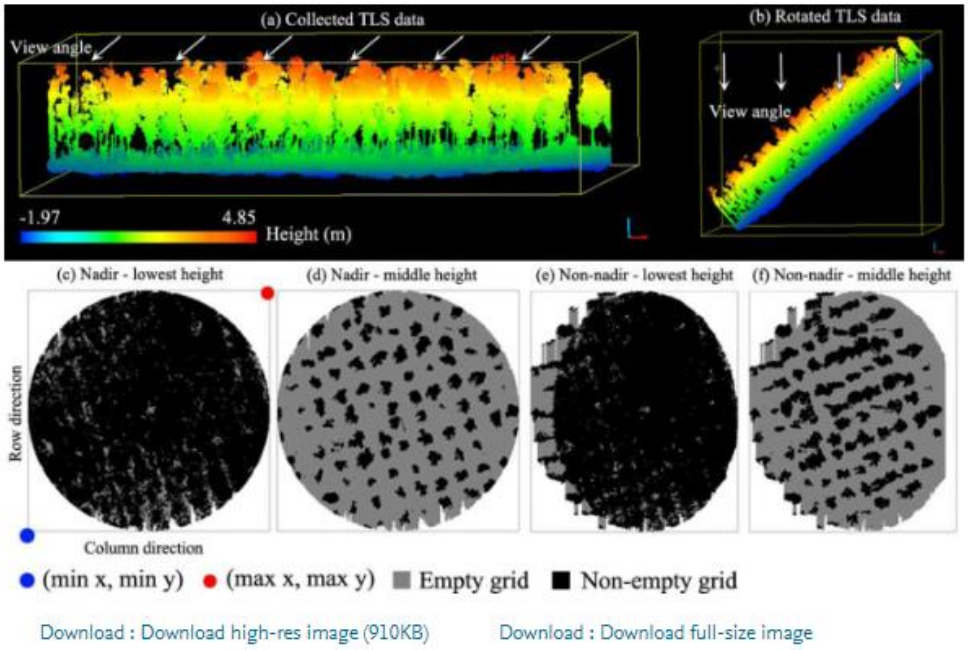

Download : Download high-res image (910KB) Download : Download full-size image

Fig. 3. Illustrations show the method of retrieving the DGF. Plot3 in 2017 at the BM site is used as an example. Inset (a) shows the collected TLS data, and inset (b) shows how the TLS data are rotated according to the view angle, with VZA and VAA set at 40° and 90°, respectively, as an example. The heights in insets (a) and (b) indicate the z value of the collected data. Insets (c) and (d) show how to obtain the numbers of empty and non-empty grids at different heights (i.e., lowest, middle) in the nadir direction based on the collected TLS data from panel (a). Insets (e) and (f) show how to obtain the numbers of empty and non-empty grids at different heights (i.e., lowest, middle) in the non-nadir direction based on the rotated TLS data from panel (b). The middle height is calculated as (highest-lowest)/2.

3rd Aug

Smith, M. N., Stark, S. C., Taylor, T. C., Ferreira, M. L., de Oliveira, E., Restrepo-Coupe, N., ... & Saleska, S. R. (2019). Seasonal and drought-related changes in leaf area profiles depend on height and light environment in an Amazon forest. *New Phytologist*, *222*(3), 1284-1297.

Summary

- Seasonal dynamics in the vertical distribution of leaf area index (LAI) may impact the seasonality of forest productivity in Amazonian forests. However, until recently, fine-scale observations critical to revealing ecological mechanisms underlying these changes have been lacking.
- To investigate fine-scale variation in leaf area with seasonality and drought we conducted monthly ground-based LiDAR surveys over 4 yr at an Amazon forest site. We analysed temporal changes in vertically structured LAI along axes of both canopy height and light environments.
- Upper canopy LAI increased during the dry season, whereas lower canopy LAI decreased. The low canopy decrease was driven by highly illuminated leaves of smaller trees in gaps. By contrast, understory LAI increased concurrently with the upper canopy. Hence, tree phenological strategies were stratified by height and light environments. Trends were amplified during a 2015–2016 severe El Niño drought.
- Leaf area low in the canopy exhibited behaviour consistent with water limitation. Leaf loss from short trees in high light during drought may be associated with strategies to tolerate limited access to deep soil water and stressful leaf environments. Vertically and environmentally structured phenological processes suggest a critical role of canopy structural heterogeneity in seasonal changes in Amazon ecosystem function.

Leaf area, drought, multi-layer, seasonal variation

2nd Aug

Hochberg, U., Rockwell, F. E., Holbrook, N. M., & Cochard, H. (2018). Iso/anisohydry: a plant–environment interaction rather than a simple hydraulic trait. *Trends in plant science*, *23*(2), 112-120.

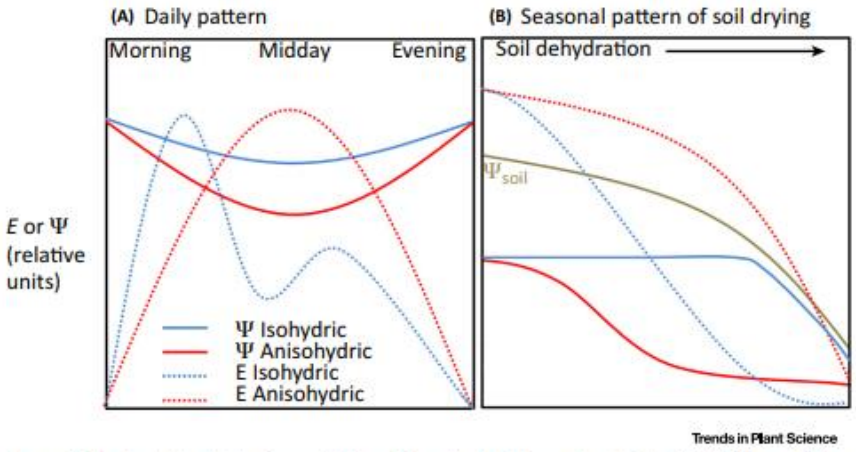

Figure 1. The Iso/Anisohydric Concept (A) as Described in Berger Lendelfeldt (1936) [1] and (B) as Commonly Described Today (Tardieu and Simmoneau, 1998 [3]). Berger Lendelfeldt made use of the terms to distinguish between the daily patterns of transpiration (*E*) and water potential (Ψ). In its modern use the terminology normally refers to the relationship between the soil water potential (Ψ_{soil}) and the minimal daily leaf water potential (Ψ_{min}) in datasets collected over long periods.

Glossary

Ψ: water potential.
Ψ_l: leaf water potential.
Ψ_{crit}: the critical leaf water potential the plant is avoiding, evident through stomatal closure.
Ψ_{min}: minimum daily leaf water potential.
Ψ_{soil}: soil water potential.
Ψ_{PD}: pre-dawn leaf water potential – a common proxy for Ψ_{soil}.
Ψ_{TLP}: the leaf water potential at turgor loss point.
$\Delta\Psi$: the difference between Ψ_{min} and Ψ_{PD}.
σ: slope of the $\Psi_{min} \sim \Psi_{soil}$ regression.
A_{max}: maximal assimilation.
E_{max}: maximal transpiration.
g_s: stomatal conductance.
***k*:** hydraulic conductance of the soil to leaf flow pathway.
***k*(Ψ_{soil}):** the response function of *k* to Ψ_{soil}.
k_{plant}: plant hydraulic conductance.

Table 1. The Variability of the Iso/Anisohydric Terminology with Notable Mentions

Definition	Isohydric	Anisohydric	Refs
Daily fluctuation in leaf water content or water potential in response to VPD	'Small' fluctuations	'Large' fluctuation	[1]
The ability (or its lack) to maintain constant Ψ_{MD} when Ψ_{soil} declines	Constant Ψ_{MD} in response to decreasing Ψ_{soil}	Decreasing Ψ_{MD} in response to decreasing Ψ_{soil}	[2,3]
Daily $\Delta\Psi = \Psi_{PD} - \Psi_{MD}$	'Small' $\Delta\Psi$	'Large' $\Delta\Psi$	[5]
Analysis of the regression of g_s versus Ψ_{min} or Ψ_{soil}	Stomatal closure at low $\Psi_{min/soil}$	Stomatal closure at high $\Psi_{min/soil}$	[9]
σ (the slope of Ψ_{MD} vs Ψ_{PD})	$\sigma < 1$	$\sigma > 1$	[6]
Hydroscape area: area of triangle bounded by the regression line, *y* axis, and 1:1 line in a plot of Ψ_{MD} versus Ψ_{MD}	'Small' hydroscape area	'Large' hydroscape area	[25]

ISOHYDRIC VS ANISOHYDRIC !

1st Aug

Barratt, G. E., Sparkes, D. L., McAusland, L., & Murchie, E. H. (2021). Anisohydric sugar beet rapidly responds to light to optimize leaf water use efficiency utilizing numerous small stomata. *AoB Plants*, *13*(1), plaa067.

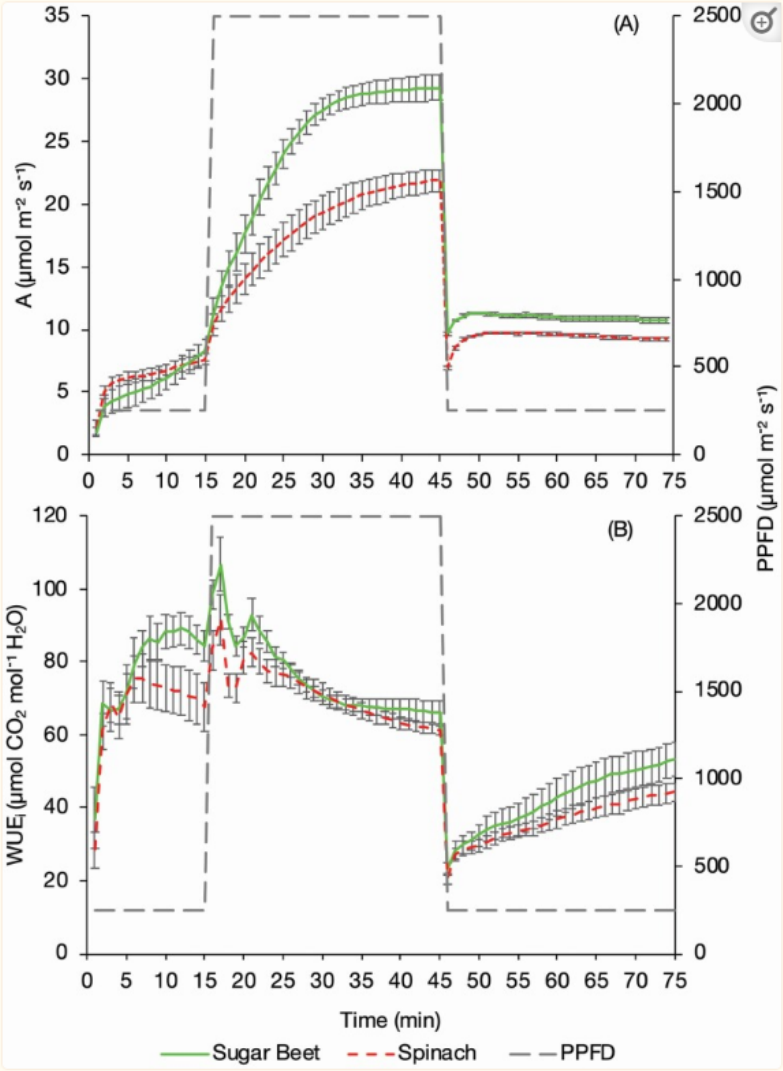

Figure 4.

The assimilation (A) and WUE_i (B) of sugar beet and spinach plants exposed to changing PPFD. Plants were exposed to a PPFD of 250 µmol m^{-2} s^{-1} for 15 min, 2500 µmol m^{-2} s^{-1} for 30 min and 250 µmol m^{-2} s^{-1} for 30 min, measured using an infrared gas analyser (LI-6800, LI-COR, Lincoln, NE, USA) with measurements logged every minute. Error bars show SE ± n = 8 sugar beet and 8 spinach.

4th July

Inamullah, & Isoda, A. (2005). Adaptive responses of soybean and cotton to water stress II. Changes in CO2 assimilation rate, chlorophyll fluorescence and photochemical reflectance index in relation to leaf temperature. *Plant Production Science*, *8*(2), 131-138.

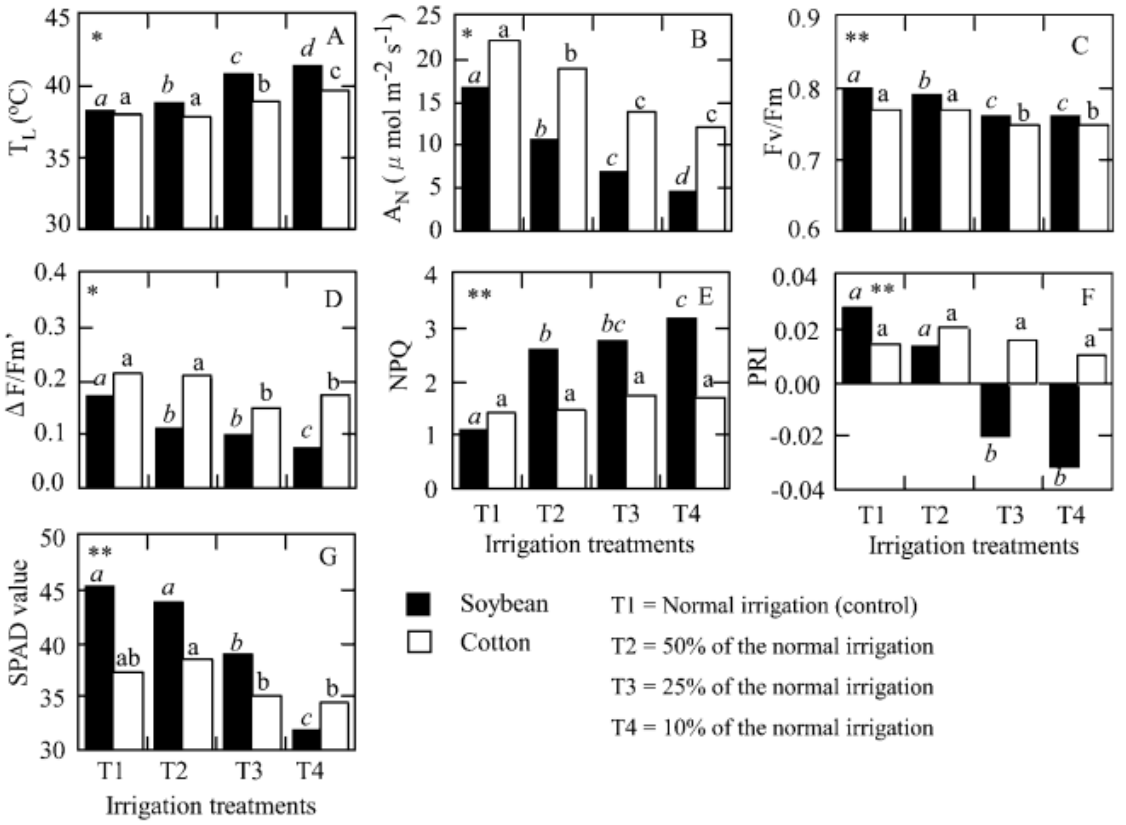

Columns representing the same crop having different letters are significantly different according to Duncan's Multiple Range Test. * and ** represent significance of the differences in the crop x irrigation interaction at 5% and 1% levels of probability, respectively.

Fig. 1. Leaf temperature (T_L, (A)), CO_2 assimilation rate (A_N, (B)), maximum quantum yield of PSII (Fv/Fm, (C)), actual quantum yield of PSII (ΔF/Fm', (D)), non-photochemical quenching (NPQ, (E)), photochemical reflectance index (PRI, (F)), and chlorophyll contents (SPAD value, (G)) in soybean and cotton under various irrigation treatments. Columns except in (C) and (G) represent means of the measurements taken in the morning (0900 hr), noon (1200 hr) and afternoon (1500 hr).

3rd July

Anderson-Teixeira, K. J., & Kannenberg, S. A. (2022). What drives forest carbon storage? The ramifications of source–sink decoupling. *New Phytologist*.

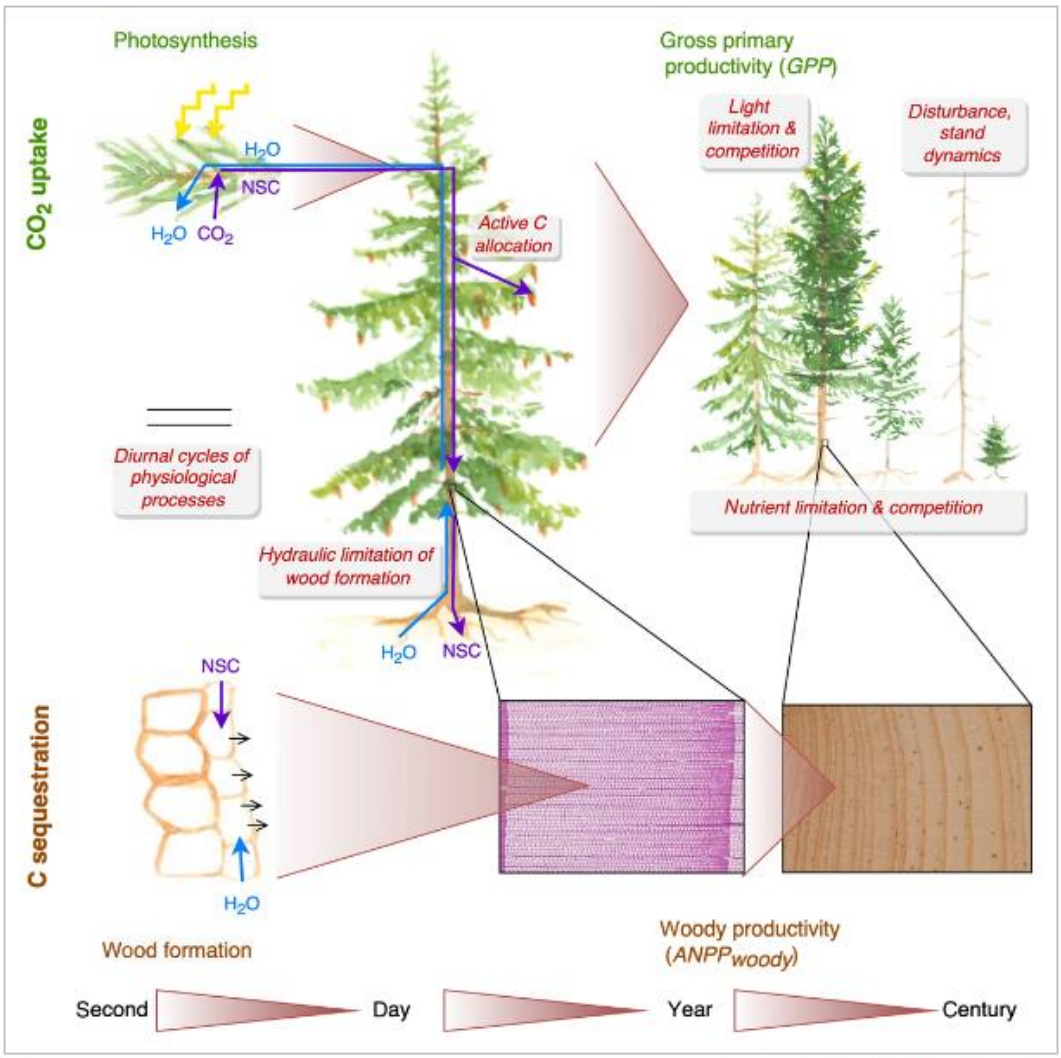

Fig. 2 Open in figure viewer | PowerPoint

Schematic summarizing sources of decoupling between CO_2 uptake and carbon (C) sequestration across various time scales. Across scales, various processes (text boxes) decouple C sequestration (wood formation or woody productivity, $ANPP_{woody}$, on the ecosystems scale) from CO_2 uptake (photosynthesis or gross primary productivity, GPP, on the ecosystems scale). Shaded wedges indicate integration across time and space. Tree ring images courtesy of Elisabet Martínez-Sancho (close-up of annual ring) and Steven A. Kannenberg (annual rings). Watercolour paintings by Kristina J. Anderson-Teixeira.

2nd July

Houtmeyers, S., & Brunner, A. (2022). Individual tree growth responses to coinciding thinning and drought events in mixed stands of Norway spruce and Scots pine. *Forest Ecology and Management*, *522*, 120447.

Highlights

- Growth trends before and after thinning were accounted for when quantifying drought responses.
- Neighborhood species composition did not affect drought responses at low stand density.
- Suppressed spruce trees had lower drought responses compared to dominant trees.

1st July

Liu, Z., Zhao, F., Liu, X., Yu, Q., Wang, Y., Peng, X., ... & Lu, X. (2022). Direct estimation of photosynthetic CO2 assimilation from solar-induced chlorophyll fluorescence (SIF). *Remote Sensing of Environment*, *271*, 112893.

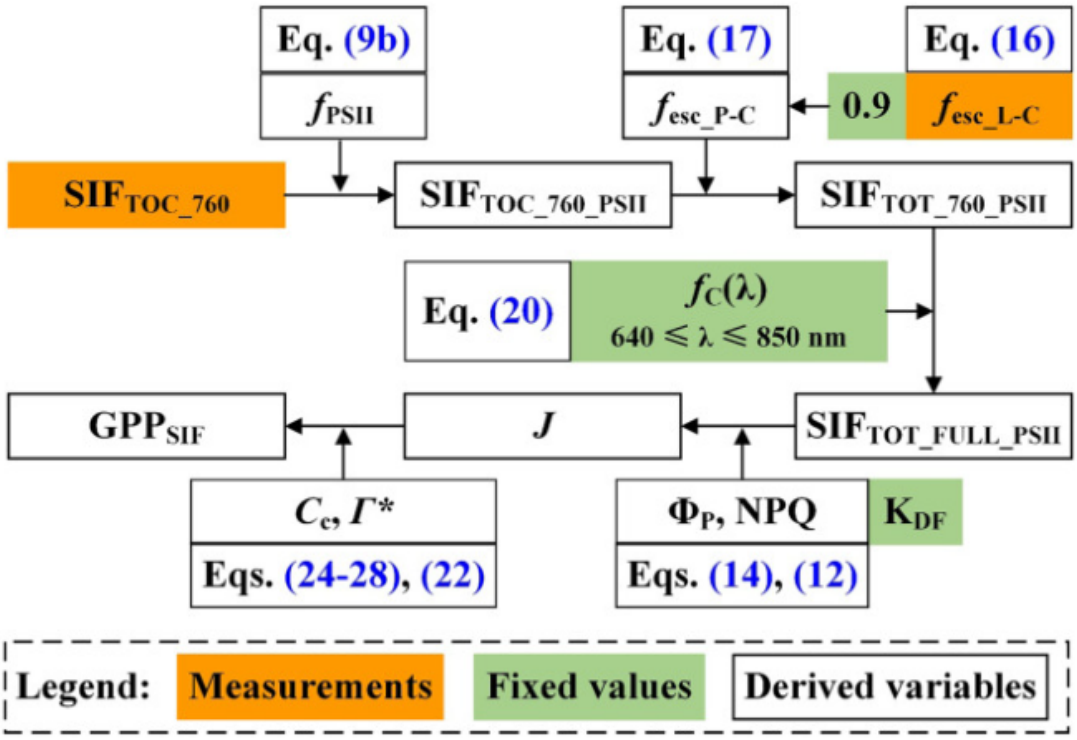

Download : Download high-res image (273KB) Download : Download full-size image

Fig. 2. Flowchart for quantifying canopy CO_2 assimilation from solar-induced fluorescence (SIF). SIF_{TOC_760}, top-of-canopy (TOC) SIF at 760 nm; f_{PSII}, photosystem II (PSII) contribution to SIF_{TOC_760}; $SIF_{TOC\_760\_PSII}$, contribution of PSII to TOC SIF at 760 nm; $f_{esc\_P\text{-}C}$, the probability that a SIF photon escapes from the PSII light reactions to the top of the canopy; $f_{esc\_L\text{-}C}$, the probability of a fluorescence photon escaping from leaf level to canopy level; 0.9, the escape probability of SIF photon from the photosystems to the leaf surface; $SIF_{TOT\_760\_PSII}$, total SIF emitted from all leaves in the canopy at photosystem level at 760 nm; $f_C(\lambda)$, the conversion ratio of $SIF_{TOT\_760\_PSII}$ to $SIF_{TOT\_\lambda\_PSII}$ at a given wavelength λ ($640 \leq \lambda \leq 850$ nm); $SIF_{TOT\_FULL\_PSII}$, broadband total (all leaves in the canopy) SIF flux density emitted by PSII; Φ_P, the quantum yield of photochemical quenching in PSII; NPQ, nonphotochemical quenching; J, linear electron transport; Γ^*, chloroplastic compensation point of CO_2; C_c, Chloroplastic CO_2 partial pressure; GPP_{SIF}, gross primary productivity deriving from SIF observations.

4th June

LI, S. L., TAN, T. T., FAN, Y. F., RAZA, M. A., WANG, Z. L., WANG, B. B., ... & Feng, Y. A. N. G. (2022). Response of leaf stomatal and mesophyll conductance to abiotic stress factors. *Journal of Integrative Agriculture*.

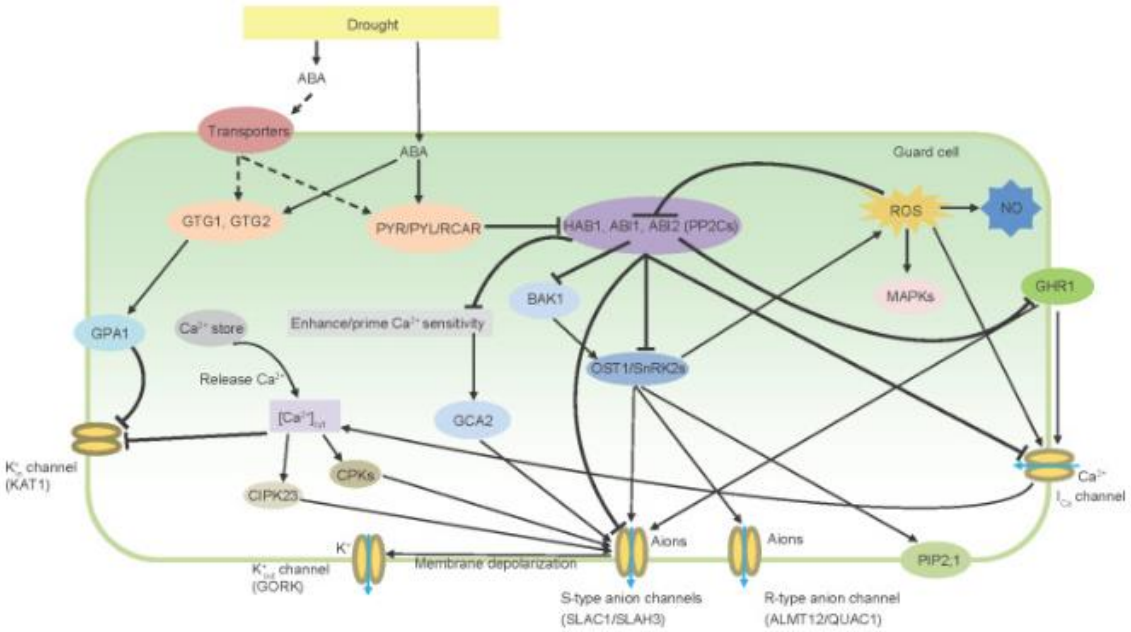

Download : Download high-res image (301KB) Download : Download full-size image

Fig. 2. Mechanism of the rapid regulation of stomatal closure by abscisic acid (ABA). GTG1, G-protein coupled receptor (GPCR)-type G proteins 1; GTG2, G-protein coupled receptor (GPCR)-type G proteins 2; PYR/PYL/RCAR, pyrabactin resistance/pyrabactin resistance 1 like/regulatory component of ABA receptor; GPA1, G proteinlpha subunit; KAT1, potassium channel in Arabidopsis thaliana 1; PP2Cs, type 2Cs protein phosphatase; ABI1, ABA-insensitive 1; ABI2, ABA-insensitive 2; HAB1, homology to ABI1; BAK1, brassinosteroid-insensitive 1 associated receptor kinase 1; OST1, open stomata 1; SnRK2s, sucrose non-fermenting 1-related protein kinase 2s; GCA2, growth controlled by abscisic acid 2; CPKs, calcium-dependent protein kinase; CIPK23 CBL-interacting protein kinase 23; ROS, reactive oxygen species; MAPKs, mitogen-activated protein kinases; NO, nitric oxide; GHR1, guard cell hydrogen peroxide-resistant 1; I_{Ca}, Ca^{2+}-permeable non-selective cation; $[Ca^{2+}]_{cyt}$, Ca^{2+} in cytosolic; GORK, guard cell outward rectifying K^+ channel.

3rd June

Zeng, L., Wardlow, B. D., Xiang, D., Hu, S., & Li, D. (2020). A review of vegetation phenological metrics extraction using time-series, multispectral satellite data. *Remote Sensing of Environment*, *237*, 111511.

Table 2. Summary of common data smoothing methods.

	Description	Classification	Processing window	Reference
Maximum value compositing (MVC)	Selecting the highest value to represent the condition for a certain period	Empirical Method	Local	Holben (1986)
Locally weighted regression	Estimating a regression surface by fitting a function of the independent variables locally	Filtering method	Local	Cleveland and Devlin (1988)
Best Index Slope Extraction (BISE)	The decrease only accepted if there is no point in a sliding period with a value greater than a certain threshold	Empirical Method	Local	(Viovy et al., 1992; Lovell and Graetz, 2001)
Fast Fourier transform	Using a least squares method to fit the first three harmonics.	Data transformation	Whole	Sellers et al. (1994)
Empirical mode decomposition	Decomposition into IMFs by "sifting"	Data transformation	Whole	Huang et al. (1998)
Temporal Window Operation (TWO)	Apply linear interpolation to remove low NDVI value within a defined temporal window.	Empirical Method	Local	(Park et al., 1999)
Harmonic ANalysis of Time Series (HANT)	Decomposes into a series of trigonometric functions	Data transformation	Whole	Roerink et al. (2000)
Discrete Fourier Transform (DFT)	Decompose the temporal data to the frequency domain	Data transformation	Whole	Moody and Johnson (2001)
Asymmetrical Gaussian (AG) function-fitting	Fitting to AG Functions	Curve fitting	Local	Jönsson and Eklundh (2002)

Logistic function-fitting	Fitting to Logistic function with different options parameters.	Curve fitting	Local	(Beck et al., 2006; Fisher et al., 2006; Zhang et al., 2003; Elmore et al., 2012; Cao et al., 2015; Zhang, 2015)
Whitaker	Fitted by penalized least square regression	Curve fitting	Whole	Eilers (2003)
Savitzky–Golay filter	Savitzky–Golay filter with iterations to the upper envelope or flexible window	Curve fitting	Local	(Chen et al., 2004; Verger et al., 2011)
Quadratic function-fitting	Simple regression models describing NDVI as a quadratic function of accumulated growing degree-days	Curve fitting	Local	de Beurs and Henebry (2004)
Wavelet based Filter	Decomposed to linear combinations of wavelet functions	Data transformation	Whole	Sakamoto et al. (2005)
Mean-value iteration filter	Iteratively compares and replaces with average value if it is above a certain threshold	Empirical Method	Local	Ma and Veroustraete (2006)
Locally adjusted cubic-spline	Determine local smoothing parameter by the local curvature of time series.	Curve fitting	Local	Chen et al. (2006)
Non-classical high order Fourier Transform	Applying high-order Fourier with roughness damping	Data transformation	Whole	Hermance (2007)
High-Order Annual Splines	Applying annual high-order polynomial splines with roughness damping	Curve fitting	Local	Hermance et al. (2007)
Iterative Interpolation	Iteratively compares to an average of different years and replaces with average value	Empirical Method	Local	Julien and Sobrino (2010)

Changing-weight filter method	Apply a three-point changing-weight filter based on local minimum/maximum points in time series	Empirical Method	Local	Zhu et al. (2012)
compound smoother RMMEH	Include several operations, such as running weighted moving average, maximum operation, arithmetic average, medians smoother	Empirical Method	Local	Jin and Xu (2013)
Parametric Double Hyperbolic Tangent model	Apply a seven-parameters hyperbolic tangent model to fit the asymmetric time-series curves	Curve fitting	Local	Meroni et al. (2014)
Spatial-temporal Savitzky-Golay (STSG)	Employs both neighboring pixels and multi-year data for noise reduction	Curve fitting	Local	Cao et al. (2018)
Shape-Prior-based method	Based on box constrained separable least squares fits combined with seasonal shape priors	Curve fitting	Local	Jönsson et al. (2018)

SOS and EOS estimation methods!

2nd June

Verrelst, J., Camps-Valls, G., Muñoz-Marí, J., Rivera, J. P., Veroustraete, F., Clevers, J. G., & Moreno, J. (2015). Optical remote sensing and the retrieval of terrestrial vegetation bio-geophysical properties–A review. *ISPRS Journal of Photogrammetry and Remote Sensing*, *108*, 273-290.

Abstract

Forthcoming superspectral satellite missions dedicated to land monitoring, as well as planned imaging spectrometers, will unleash an unprecedented data stream. The processing requirements for such large data streams involve processing techniques enabling the spatio-temporally explicit quantification of vegetation properties. Typically retrieval must be accurate, robust and fast. Hence, there is a strict requirement to identify next-generation bio-geophysical variable retrieval algorithms which can be molded into an operational processing chain. This paper offers a review of state-of-the-art retrieval methods for quantitative terrestrial bio-geophysical variable extraction using optical remote sensing imagery. We can categorize these methods into (1) *parametric regression*, (2) *non-parametric regression*, (3) *physically-based* and (4) *hybrid methods*. Hybrid methods combine generic capabilities of physically-based methods with flexible and computationally efficient methods, typically non-parametric regression methods. A review of the theoretical basis of all these methods is given first and followed by published applications. This paper focusses on: (1) retrievability of bio-geophysical variables, (2) ability to generate multiple outputs, (3) possibilities for model transparency description, (4) mapping speed, and (5) possibilities for uncertainty retrieval. Finally, the prospects of implementing these methods into future processing chains for operational retrieval of vegetation properties are presented and discussed.

Related to models.

1st June

Spafford, L., Le Maire, G., MacDougall, A., De Boissieu, F., & Féret, J. B. (2021). Spectral subdomains and prior estimation of leaf structure improves PROSPECT inversion on reflectance or transmittance alone. *Remote Sensing of Environment*, *252*, 112176.

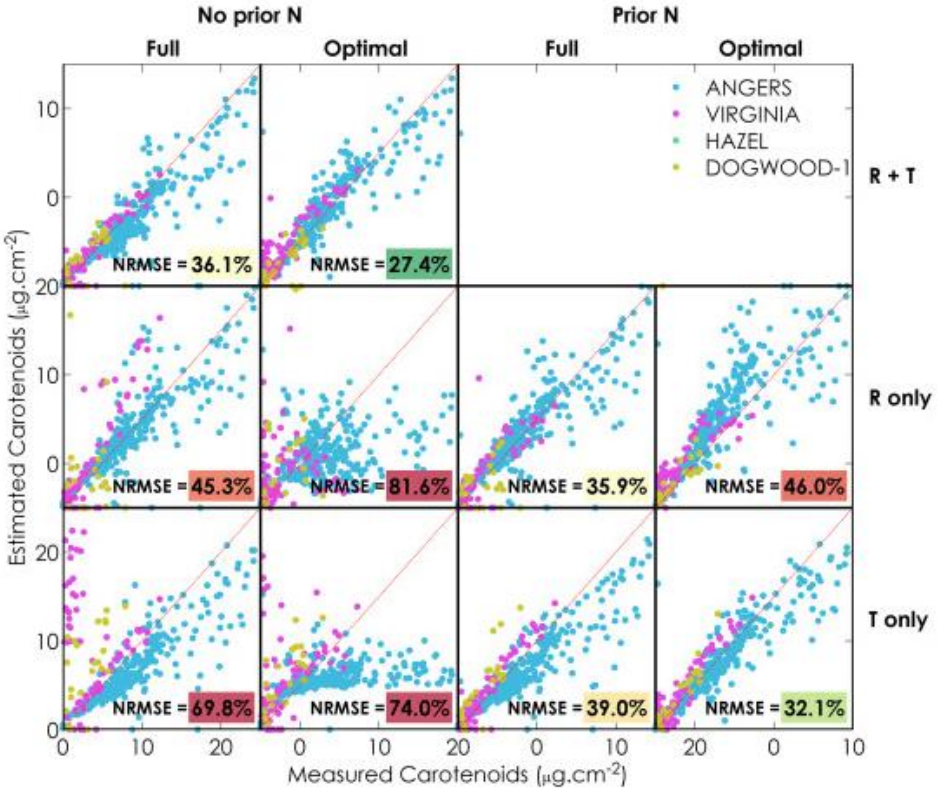

Download : Download high-res image (947KB) Download : Download full-size image

Fig. 4. Estimation of Cxc using ten different strategies for PROSPECT inversion. NRMSE is provided for the compiled dataset, and the background color for NRMSE value indicates if the performances are improved (green) or worsened (red) compared to the inversion using both reflectance and transmittance over the full spectral domain without prior estimation of N. (For interpretation of the references to color in this figure legend, the reader is referred to the web version of this article.)

4th May

Vicari, M. B., Pisek, J., & Disney, M. (2019). New estimates of leaf angle distribution from terrestrial LiDAR: Comparison with measured and modelled estimates from nine broadleaf tree species. *Agricultural and forest meteorology*, *264*, 322-333.

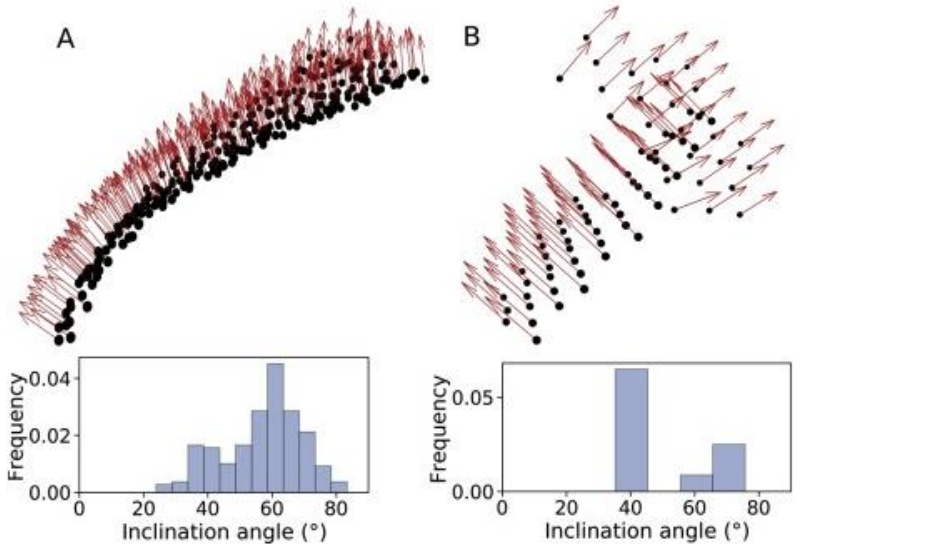

Download : Download high-res image (343KB) Download : Download full-size image

Fig. 7. Normal vectors calculated for a single leaf from field scanned *Diospyros lotus* point cloud (A) and from two neighboring leaves from TICO2 simulated point cloud (B). Respective leaf angle distributions calculated from point-wise angle are shown under each respective set of points.

3rd May

Chen, Y., Jiao, S., Cheng, Y., Wei, H., Sun, L., & Sun, Y. (2022). LAI-NOS: An automatic network observation system for leaf area index based on hemispherical photography. *Agricultural and Forest Meteorology*, *322*, 108999.

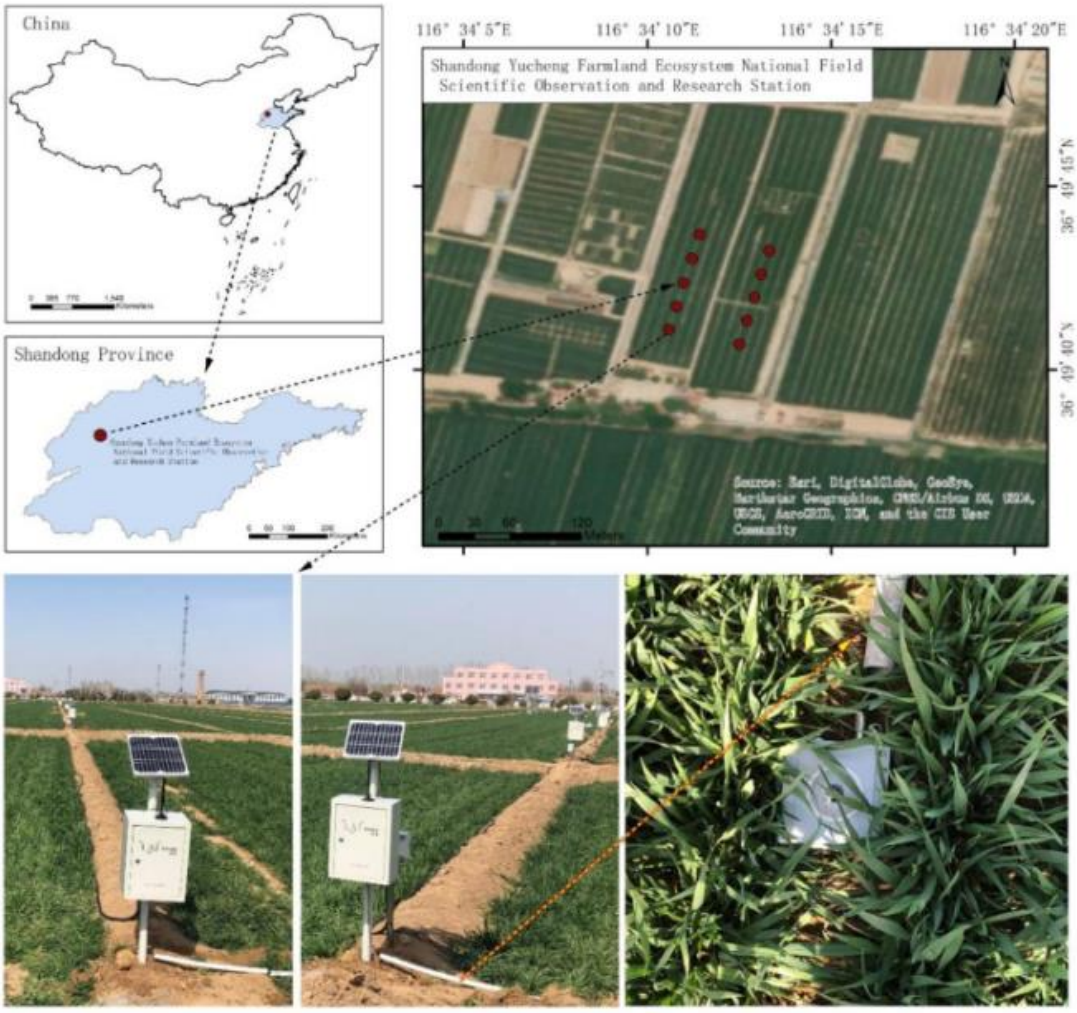

Download : Download high-res image (2MB) Download : Download full-size image

Fig. 2. Yucheng station location, node distribution, sensor node, and LAI sensor in field. The first row of images shows the study area in Yucheng County, Shandong Province, China, and the node distribution. The distance between the two columns of nodes is 50 m, and the distance between adjacent nodes within rows is 20 m. The second row of images shows the sensor node and the LAI sensor. The background image of the upper right image provided courtesy of OpenStreetMap. (color printing).

2nd May

Pisek, J., Diaz-Pines, E., Matteucci, G., Noe, S., & Rebmann, C. (2022). On the leaf inclination angle distribution as a plant trait for the most abundant broadleaf tree species in Europe. *Agricultural and Forest Meteorology*, *323*, 109030.

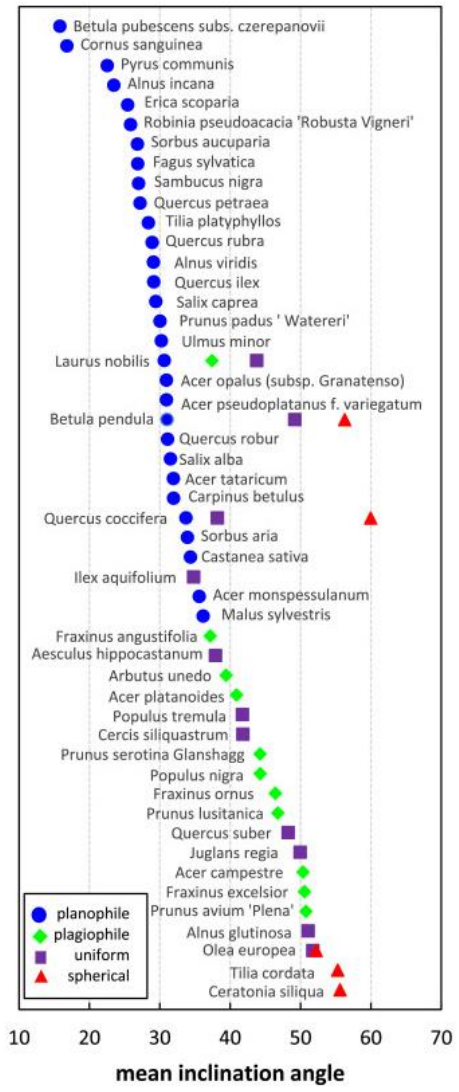

Download : Download high-res image (639KB) Download : Download full-size image

Fig. 5. 50 broadleaf tree species common to Europe reported in Table 2, ranked by mean inclination angles with indicated classic de Wit type of leaf angle distribution (planophile, pagiophile, uniform, spherical).

1st May

Cannon, J. B., Warren, L. T., Ohlson, G. C., Hiers, J. K., Shrestha, M., Mitra, C., ... & Ocheltree, T. W. (2022). Applications of low-cost environmental monitoring systems for fine-scale abiotic measurements in forest ecology. *Agricultural and Forest Meteorology*, *321*, 108973.

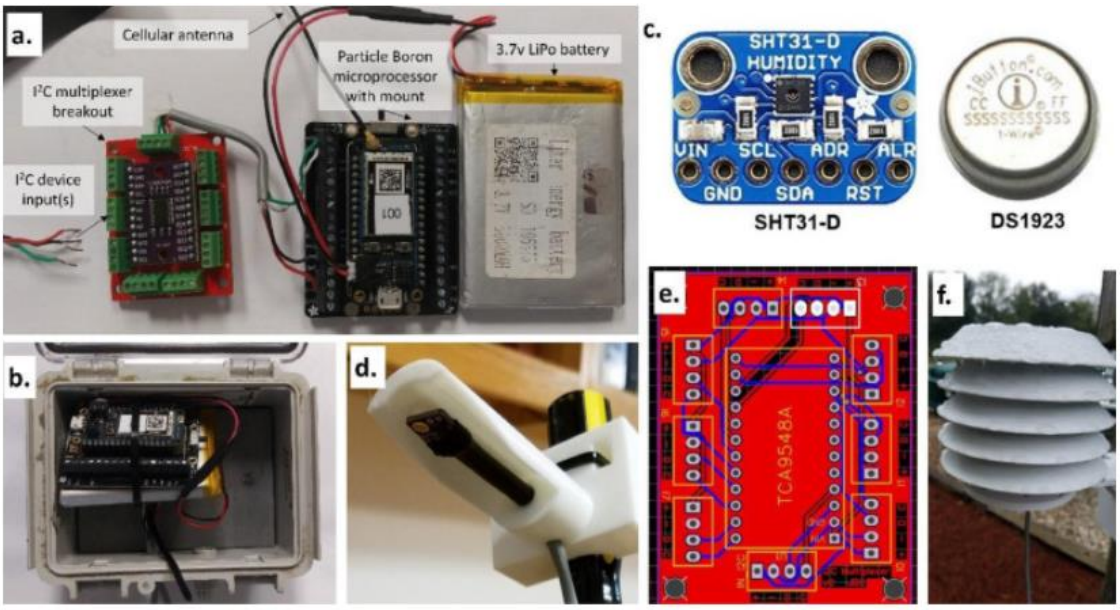

Download : Download high-res image (1MB) Download : Download full-size image

Fig. 1. (a-f) Development of environmental monitoring using open-source platforms. (a) Datalogging assembly based on Particle Boron microprocessor on a screw terminal mount powered by a 3.7V 5000 mAH LiPo battery. Custom printed circuit board (PCB, red) includes an I^2C multiplexer chip allowing up to eight identically addressed sensors. (b) Datalogging assembly installed in a weather resistant enclosure. (c) Comparison of Adafruit SHT31-D temperature and humidity sensor (left) and iButton Hygrochron (DS1932, right). (d) Minimalist radiation shield mount with installed SHT31-D sensor. (e) Custom PCB to use I^2C multiplexer with 4-pin screw terminals. (f) 5-fin radiation shield 3D printed with PETG. See Appendix and https://github.com/jbcannon/sht31-array for complete construction and deployment guide.

4th April

Kao, W. Y., & Forseth, I. N. (1992). Dirunal leaf movement, chlorophyll fluorescence and carbon assimilation in soybean grown under different nitrogen and water availabilities. *Plant, Cell & Environment*, *15*(6), 703-710.

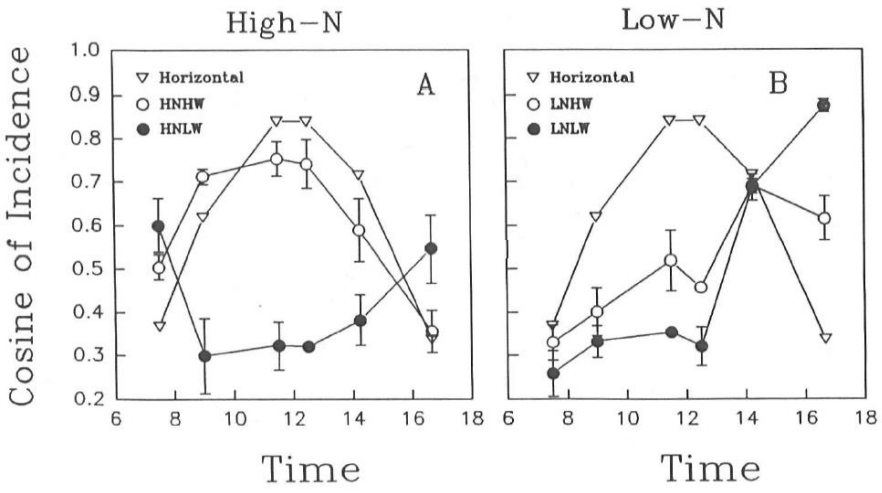

Figure 2. Diurnal courses of cosine of incidence on a horizontal surface and on heliotropic leaves of high nitrogen/high water (HNHW), high nitrogen/low water (HNLW), low nitrogen/high water (LNHW) and low nitrogen/low water (LNLW) grown soybean plants.

2 h on 7 September 1990 on four different leaflets of four different plants of each treatment. The cosine of the angle of incidence (cos i) represents the cosine of the angle between a normal to the sun's direct beam and the leaf lamina. It is a measure of the proportion of the direct beam incident on the leaf. A cos i of 1 would represent a leaf with its adaxial surface perpendicular to the direct beam, while a value of 0 would represent a leaf with its adaxial surface parallel to the direct solar beam. Cos i was calculated according to the following formula (Prichard & Forseth 1988):

$$\cos i = \cos \beta * \cos z + \sin \beta * \sin z * \cos (\alpha_s - \alpha_l)$$

where β=leaf angle from the horizontal, z=solar zenith angle, α_s=solar azimuth angle, and α_l=leaf azimuth.

Nice paper for leaf angle, fluorescence yield.

-

3rd April

Kao, W. Y., & Forseth, I. N. (1992). Responses of gas exchange and phototropic leaf orientation in soybean to soil water availability, leaf water potential, air temperature, and photosynthetic photon flux. *Environmental and Experimental Botany*, *32*(2), 153-161.

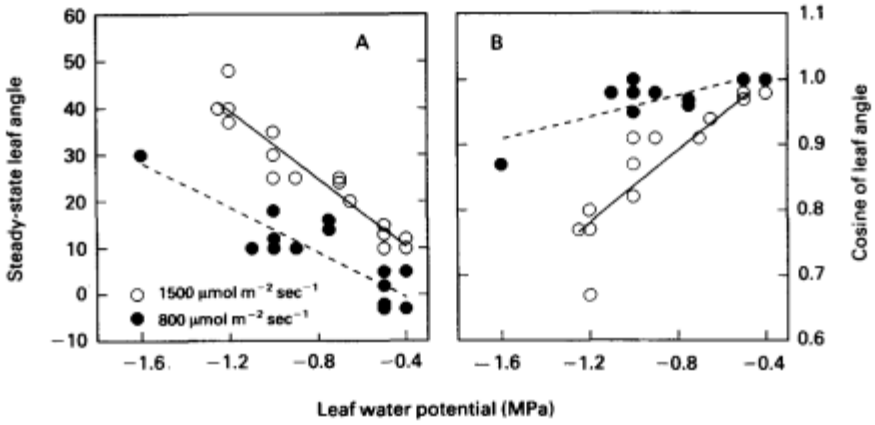

FIG. 3. The effect of *PPF* on the relationship between (A) leaf water potential and steady-state leaf angle, and (B) leaf water potential and cosine of steady-state leaf angle calculated from (A).

Leaf water potential vs leaf angle

-

2nd April

Fang, H. (2021). Canopy clumping index (CI): A review of methods, characteristics, and applications. *Agricultural and Forest Meteorology*, *303*, 108374.

Download : Download high-res image (733KB) Download : Download full-size image

Fig. 1. Foliage clumping at different hierarchical levels for needleleaf (upper) and broadleaf (lower) forests.

Nice review for the CI

-

1st April

Zeng, Y., Hao, D., Badgley, G., Damm, A., Rascher, U., Ryu, Y., ... & Chen, M. (2021). Estimating near-infrared reflectance of vegetation from hyperspectral data. *Remote Sensing of Environment*, *267*, 112723.

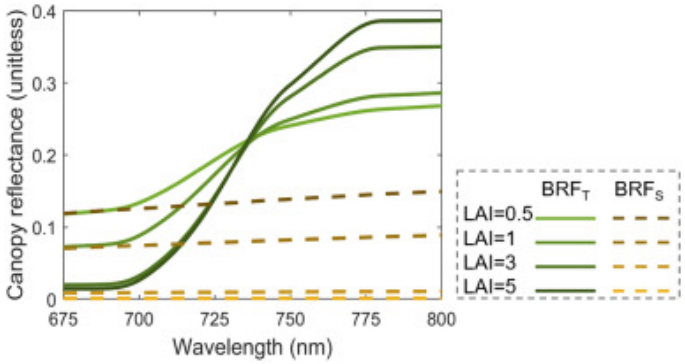

Download : Download high-res image (81KB) Download : Download full-size image

Fig. 3. Canopy-scale total reflectance (BRF_T) with increasing LAI and the same soil background (dried soil, 4-Brightest in Fig. 2), simulated by the SCOPE model. The soil single scattering contribution (BRF_S) is calculated by the product of the bidirectional gap fraction times the soil reflectance. The spectral range of 675–800 nm represents the red edge which we are interested in for the NIRvH estimation. (For interpretation of the references to colour in this figure legend, the reader is referred to the web version of this article.)

-

4th March

Gitelson, A., Viña, A., Inoue, Y., Arkebauer, T., Schlemmer, M., & Schepers, J. (2022). Uncertainty in the evaluation of photosynthetic canopy traits using the green leaf area index. *Agricultural and Forest Meteorology*, *320*, 108955.

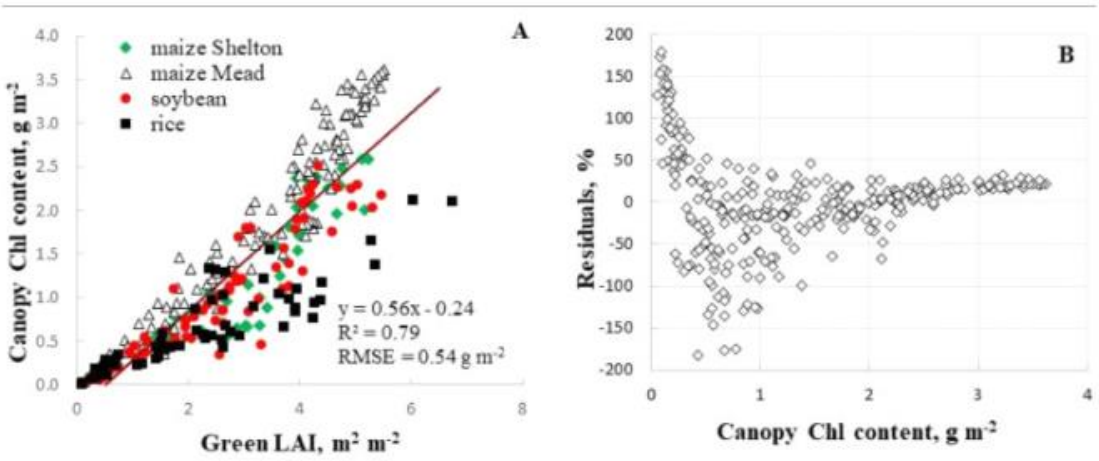

Download : Download high-res image (353KB)

Download : Download full-size image

Fig. 3. (A) Relationship between CCC and GLAI for all crops and sites evaluated; (B) residuals of this relationship for all datasets combined.

Not sure the VERY old data set is reliable, still useful, and really a novelty. However, it is also really amazing.

Green LAI vs canopy Chl

-

3rd March

Stovall, A. E., Masters, B., Fatoyinbo, L., & Yang, X. (2021). TLSLeAF: automatic leaf angle estimates from single-scan terrestrial laser scanning. *New Phytologist*, *232*(4), 1876-1892.

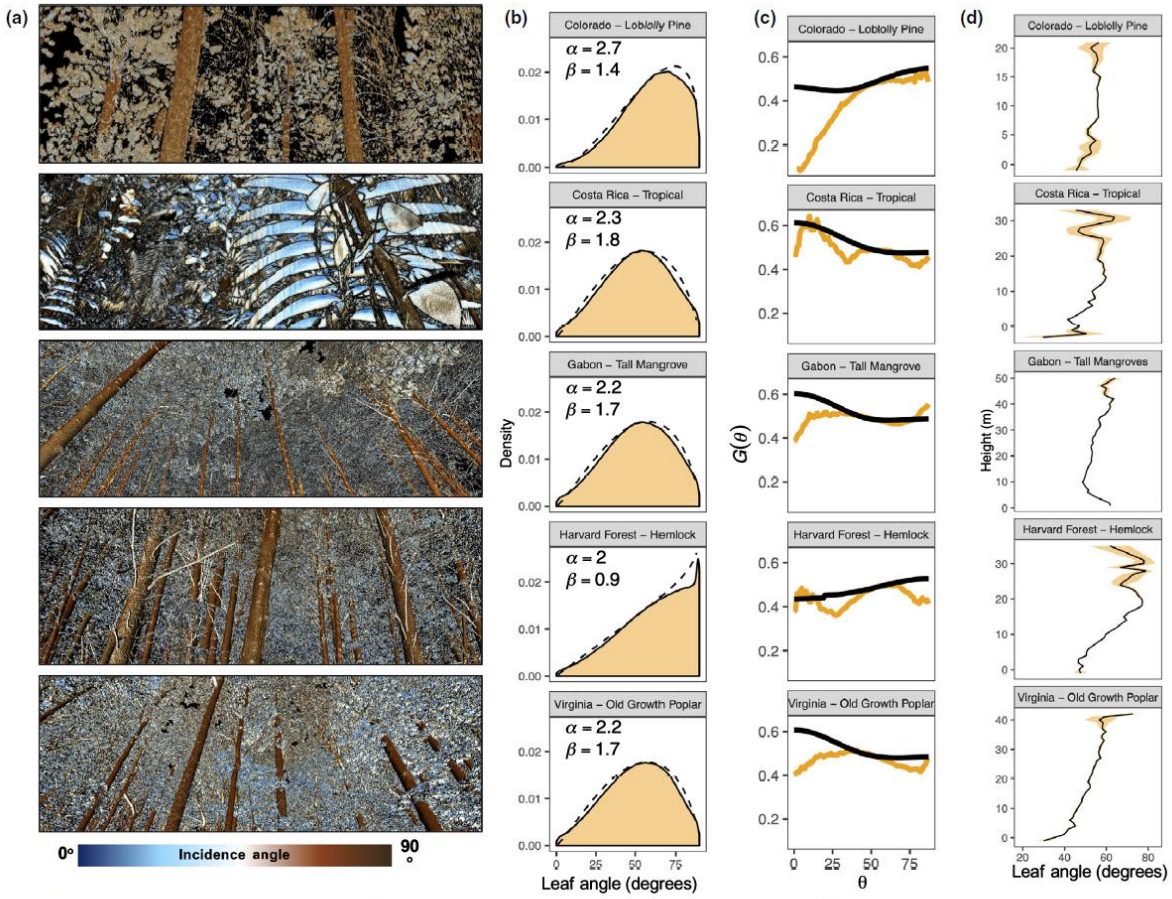

Fig. 9 The five example forested sites with derived leaf angle parameters (terrestrial laser scan subset area and angles shown in (a)) including (b) leaf angle distributions and associated beta distributions (black dotted lines; parameters shown), (c) random (black) and nonrandom (orange) *G*-functions, and (d) vertical distributions of mean leaf angle (black) with 95% confidence intervals (shaded orange).

ABout TLSLeAF

-

2nd March

Huang, Y., Zhou, C., Du, M., Wu, P., Yuan, L., & Tang, J. (2022). Tidal influence on the relationship between solar-induced chlorophyll fluorescence and canopy photosynthesis in a coastal salt marsh. *Remote Sensing of Environment*, *270*, 112865.

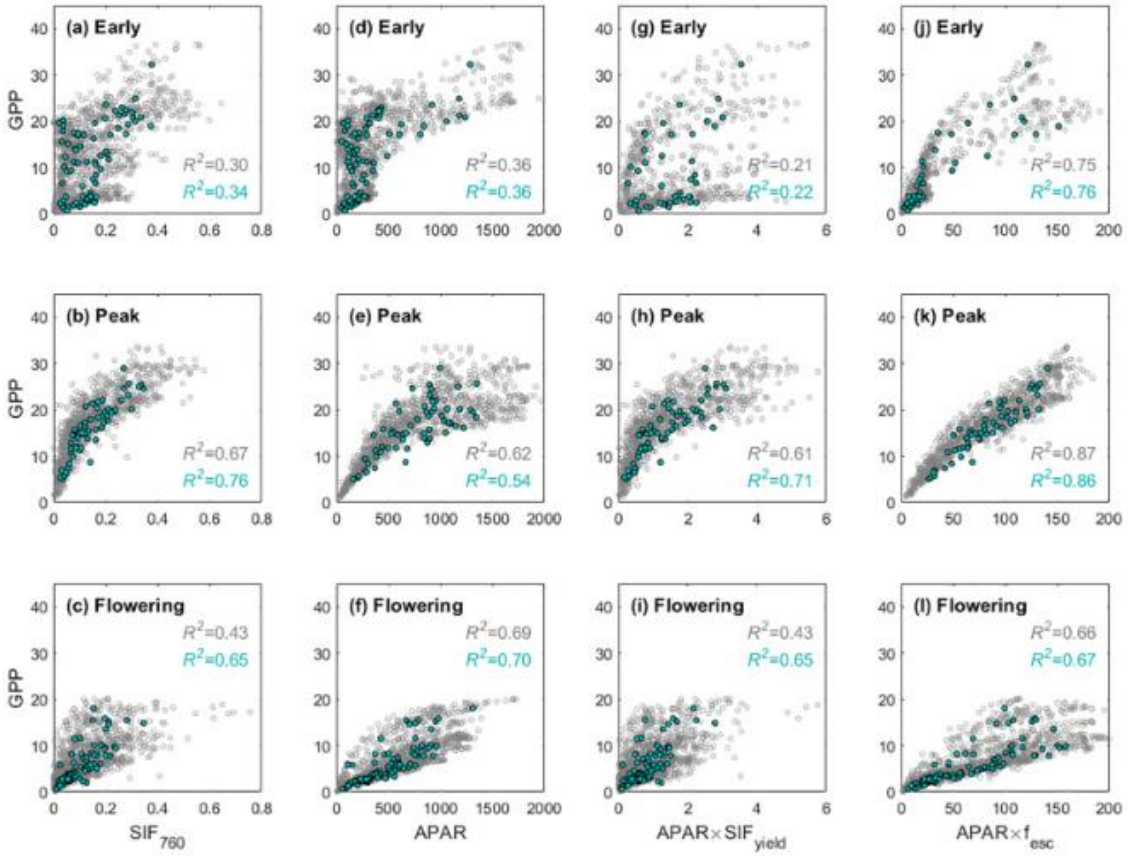

Download : Download high-res image (506KB) Download : Download full-size image

Fig. 5. Relationships between the half-hourly (grey circle) and daily averaged (green circle) gross primary productivity (GPP, μmol m^{-2} s^{-1}) and the (a–c) observed solar-induced

SIF-GPP relationship in salt marsh

-

1st March

Zhu, X., Wang, T., Skidmore, A. K., Darvishzadeh, R., Niemann, K. O., & Liu, J. (2017). Canopy leaf water content estimated using terrestrial LiDAR. *Agricultural and forest meteorology*, *232*, 152-162.

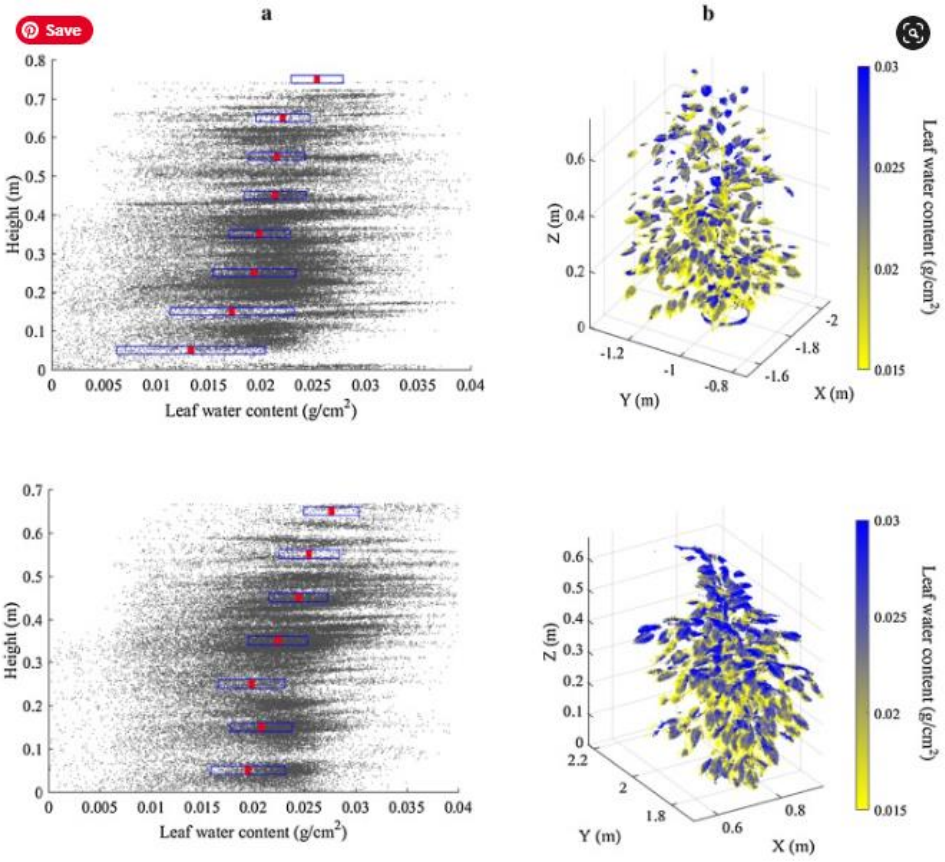

Download : Download high-res image (2MB) Download : Download full-size image

Fig. 9. Examples of leaf water content distribution of the 2 plant species (weeping fig and ficus). (a) LWC vertical distribution (The red square indicates the mean value and the blue rectangle indicates the standard deviation) and (b) LWC visualization (plants were scanned downward from the TLS). (For interpretation of the references to color in this figure legend,

About 3D leaf water content distribution.

-

4th Feb

Pierrat, Z., Magney, T., Parazoo, N. C., Grossmann, K., Bowling, D. R., Seibt, U., ... & Stutz, J. (2022). Diurnal and seasonal dynamics of solar-induced chlorophyll fluorescence, vegetation indices, and gross primary productivity in the boreal forest. *Journal of Geophysical Research: Biogeosciences*, e2021JG006588.

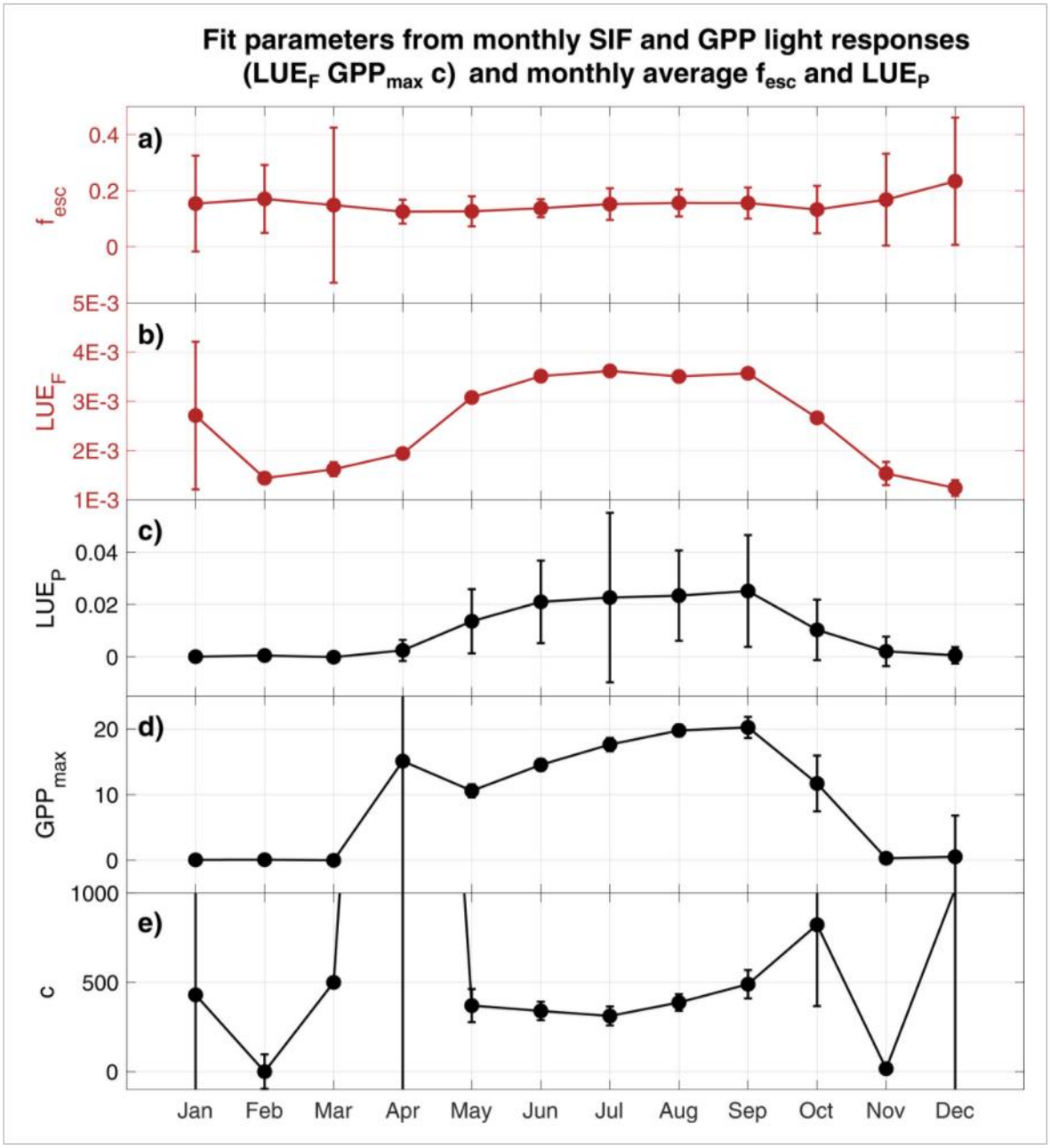

Good to see they citied my previous paper 4 times! At small temporal scales, SIF and GPP are predominantly driven by light and non-linearity between SIF and GPP is due to the light saturation of GPP. Averaged over daily and monthly scales, the relationship between SIF and GPP is linear due to a reduction in the observed PAR range. Seasonal changes in the light responses of SIF and GPP are driven by changes in light use efficiency which co-vary with changes in temperature, while illumination and canopy structure partially linearize the SIF-GPP relationship. Additionally, we find that the SIF-GPP relationship has a seasonal dependency.

-

3rd Feb

Shin, J., Kim, D., & Noh, Y. (2022). Estimation of Aerosol Extinction Coefficient Using Camera Images and Application in Mass Extinction Efficiency Retrieval. *Remote Sensing, 14*, 1224

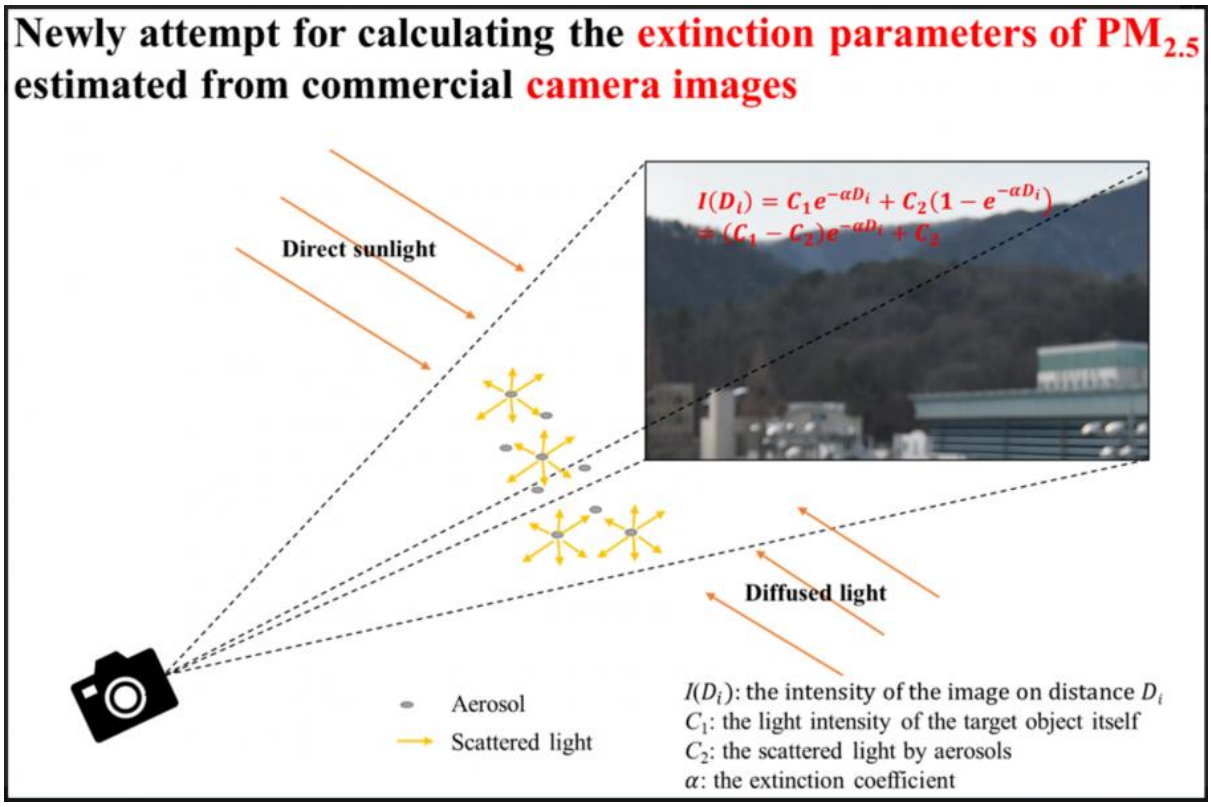

I really enjoyed their idea. Using the RGB values of pixels, we calculated the extinction coefficient and efficiency applied to the mass concentration of $PM_{2.5}$. The calculated extinction coefficient of $PM_{2.5}$ determined from the camera images had a higher correlation with the $PM_{2.5}$ mass concentration ($R^2 = 0.7$) than with the visibility data, despite the limited mass range. Finally, we identified that the method of calculating extinction parameters using the effective wavelength of RGB images could be applied to studies of changes in the atmosphere and aerosol characteristics.

-

2nd Feb

Zhang, Q., Zhang, X., Li, Z., Wu, Y., & Zhang, Y. (2019). Comparison of Bi-Hemispherical and hemispherical-conical configurations for in situ measurements of solar-induced chlorophyll fluorescence. *Remote Sensing*, *11*(22), 2642.

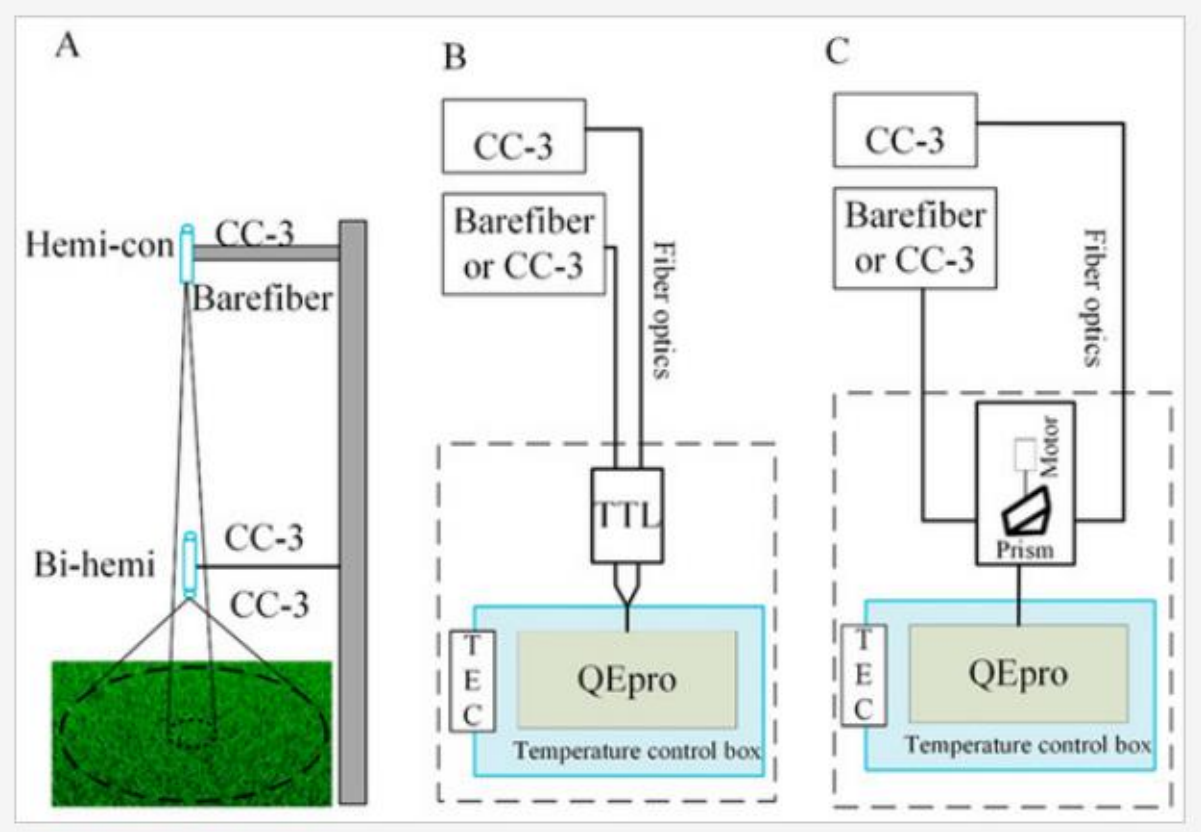

Good to see their system is working well. They found that when the target is heterogeneous, e.g., the Epipremnum aureum canopy, the values and diurnal pattern of far-red SIF derived from systems with a bi-hemi configuration were obviously different with those derived from the system with hemi-con configuration. These results demonstrate that different SIF systems are able to acquire consistent SIF for landscapes with a homogeneous canopy. However, SIF retrieved from bi-hemi and hemi-con configurations may be distinctive when the target is a heterogeneous (or discontinuous) canopy due to the different fields of view and viewing geometries.

-

1st Feb

Damm, A., Cogliati, S., Colombo, R., Fritsche, L., Genangeli, A., Genesio, L., Hanus, J., Peressotti, A., Rademske, P., Rascher, U., Schuettemeyer, D., Siegmann, B., Sturm, J., & Miglietta, F. (2022). Response times of remote sensing measured sun-induced chlorophyll fluorescence, surface temperature and vegetation indices to evolving soil water limitation in a crop canopy. *Remote Sensing of Environment, 273*, 112957

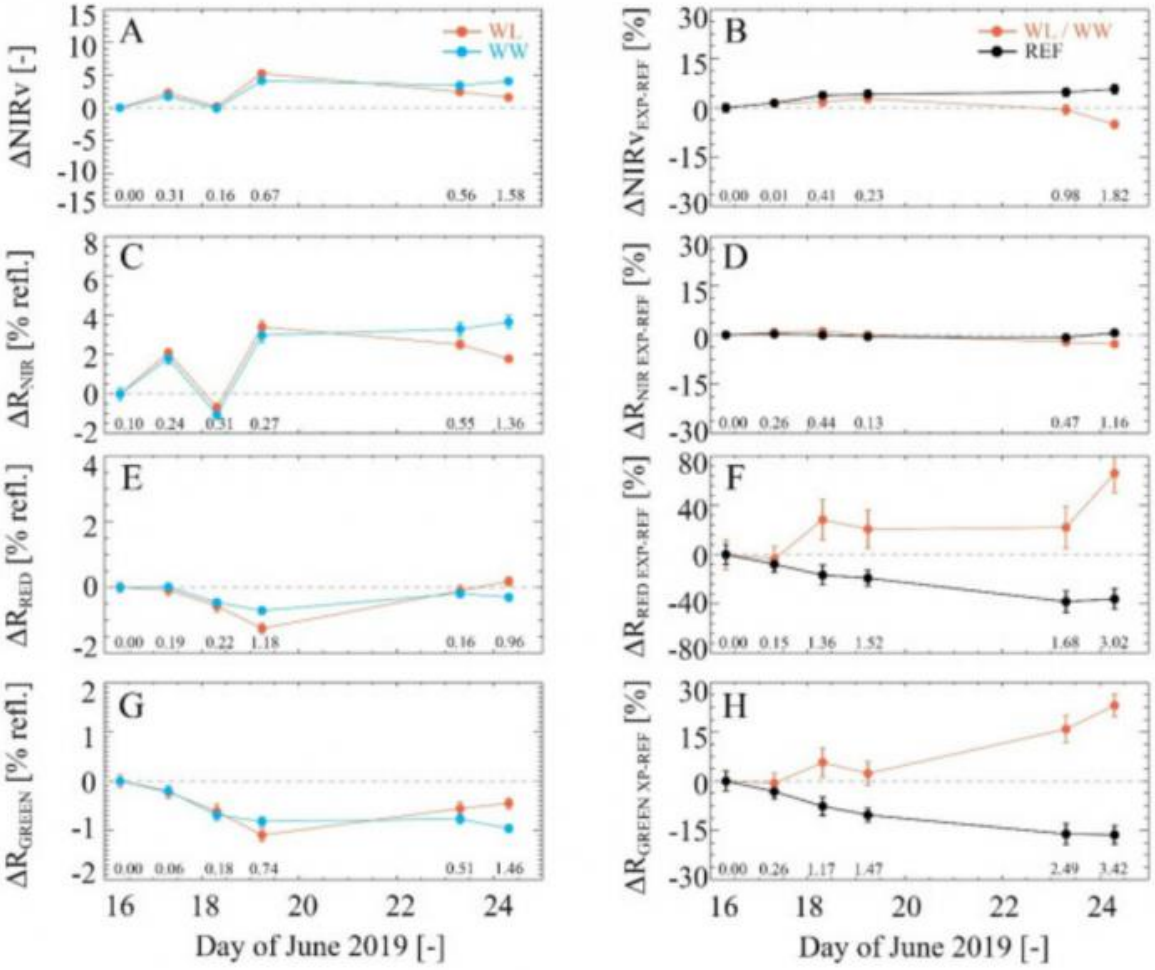

I really enjoyed this paper. I think our drought experiment result would be great contributed in this field.

-

4th Jan

Zhao, D., Hou, Y., Zhang, Z., Wu, Y., Zhang, X., Wu, L., ... & Zhang, Y. (2022). Temporal resolution of vegetation indices and solar-induced chlorophyll fluorescence data affects the accuracy of vegetation phenology estimation: A study using in-situ measurements. *Ecological Indicators*, *136*, 108673.

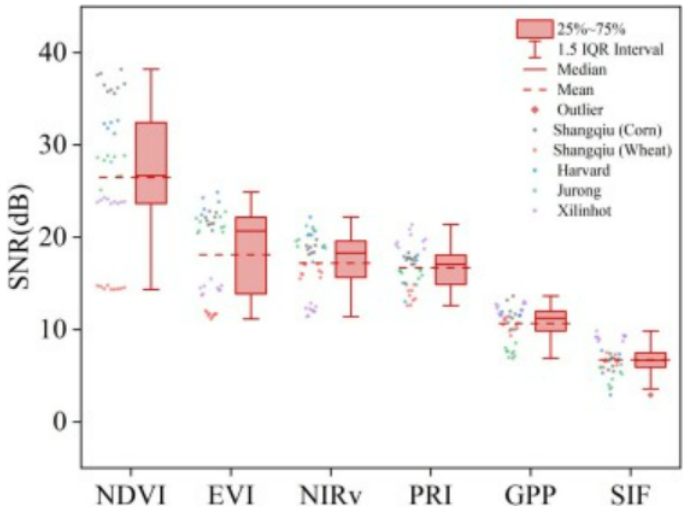

Download : Download high-res image (85KB) Download : Download full-size image

Fig. 11. Boxplots of signal–noise ratio (SNR) of different vegetation phenology indicators in LSP estimation.

SNR represents the data noise level in actual observation. The higher the SNR, the lower the data noise level in actual observation. The low SNR may lead to more uncertainties in LSP estimation, such as deformation of the growing season curve, the bias of the fitting parameters of the growing season curve, the difficulty of fitting the growing season curve, and so on. Therefore, compared with vegetation indices (NDVI, EVI, NIR_V, PRI), GPP and SIF with lower SNR can show more uncertainties in LSP estimation.

The sensitivity of SIF and GPP to temporal resolution (both observation temporal resolution (OTR) and composite temporal resolution (CTR)) in LSP estimation was higher than that of vegetation indices (NDVI, EVI, NIR_V, PRI) due to higher data noise. Furthermore, in LSP estimation, the selection of the required temporal resolution of RSD was directly related to the data quality. The results highlight the importance of the temporal resolution in LSP estimation from RSD and provide two possible insights to reduce the errors of LSP estimation. First, in the case of the appropriate data compositing strategies and very little data noise, temporal resolution (both OTR and CTR) can be considered to have little influence on LSP estimation. Second, most of the difference in sensitivity of different indicators to temporal resolution comes from external factors, including observation and model or algorithm errors, rather than the properties of indicators.

3rd Jan

Kuhlgert, S., Austic, G., Zegarac, R., Osei-Bonsu, I., Hoh, D., Chilvers, M. I., ... & Kramer, D. M. (2016). MultispeQ Beta: a tool for large-scale plant phenotyping connected to the open PhotosynQ network. *Royal Society open science*, *3*(10), 160592.

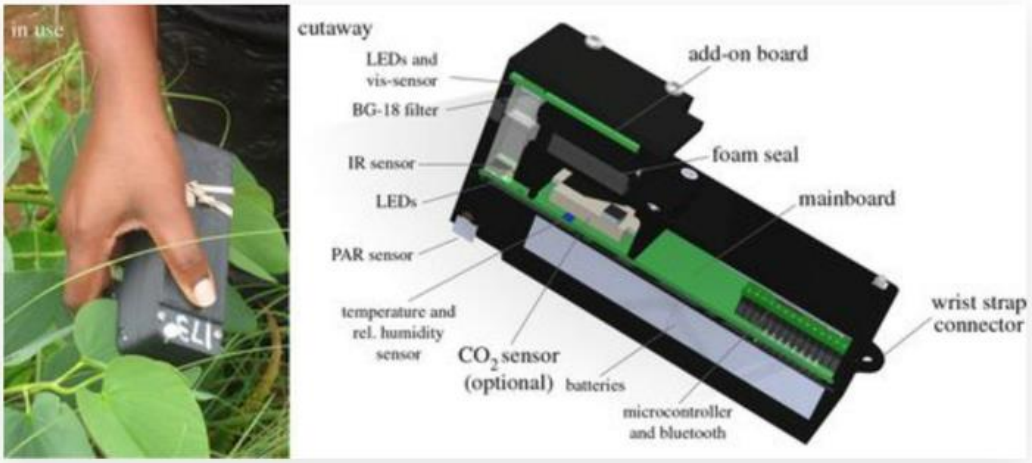

Figure 1. The MultispeQ device as used in the field and a cutaway schematic diagram. See the text for details.

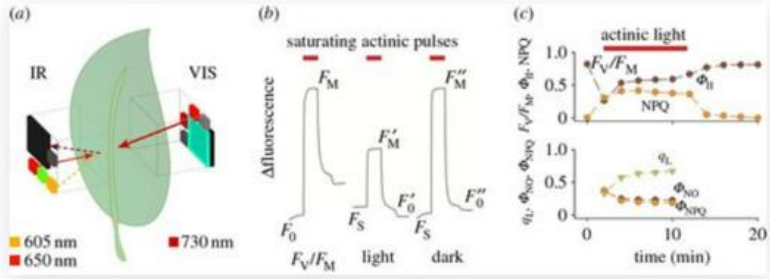

Figure 4. Example of photosynthetic parameters derived from pulse-amplitude modulation (PAM) fluorometry using MultispeQ. (*a*) LED and detector set-up to measure fluorescence-based kinetics. Shown are the light paths for the actinic illumination (650 nm, red solid arrow), fluorescence excitation (605 nm, orange dashed arrow), and far red (730 nm, dark red solid arrow) and chlorophyll fluorescence (dark brown dashed arrow). (*b*) Representative fluorescence transients in an attached *Camelina sativa* leaf. Each sequence consisting of 100 pulses of orange LED light (pulses with duration of 10 µs, emission peak at 605 nm at 100 Hz). After 50 pulses a 50 pulses long saturating flash using the 650 nm LED was given (approx. 10 000 µmol photons m^{-2} s^{-1}) followed by far-red illumination (830 nm). From left to right, traces represent transient taken in the dark-adapted state, which can be used to calculate F_V/F_M; trace taken during steady-state illumination, which can be used to estimate Φ_{II} and NPQ parameters, and about 5 min after returning the leaf to the dark, which can be used to estimate q_E and q_I. The results are very similar to those reported earlier, e.g. [31]. (*c*) Time course of fluorescence parameters were derived from measurements taken on a *Camelina sativa* leaf. After 10 min of dark adaptation, F_V/F_M was measured and the next five measurements in the presence of actinic background illumination at 100 µmol photons m^{-2} s^{-1}, followed by five sets in the dark. From the resulting fluorescence traces, F_V/F_M, quantum yield estimates for photochemistry (Φ_{II}) and NPQ (upper panel) were derived, as well as estimates of Q_A redox state (q_L), Φ_{NPQ} and non-regulatory excitation dissipation (Φ_{NO}) (lower panel).

I really like this tool! It looks really nice!

-

2nd Jan

Hao, D., Zeng, Y., Zhang, Z., Zhang, Y., Qiu, H., Biriukova, K., ... & Chen, M. (2022). Adjusting solar-induced fluorescence to nadir-viewing

provides a better proxy for GPP. *ISPRS Journal of Photogrammetry and Remote Sensing*, *186*, 157-169.

Download : Download high-res image (358KB) Download : Download full-size image

Fig. 6. The R^2 values for the linear relationships between observed/nadir/total *SIF*s for far-red and red bands and *GPP* under different *VAA*s for wheat (a-b) and corn (c-d). For each boxplot, white circles represent the mean values and grey points represent R^2 values. (For interpretation of the references to color in this figure legend, the reader is referred to the web version of this article.)

This paper found that nadir-view SIF could track GPP well. Although the viewing angle effects dominate the difference in estimating GPP between SIFnadir and SIFobs, the correlation between LUE and fesc further determines the different performance of SIFnadir and SIFtotal in estimating GPP. TROPOMI-based analysis further confirms that SIFnadir overall has higher correlations to AmeriFlux *GPP* than SIFobs for different plant functional types and shows similar performance with SIFtotal. Compared to SIFtotal, the estimation of SIFnadir independent of viewing angle effects does not require any canopy structure parameters, and thus offers promising potential for reliably estimating regional and global *GPP*.

-

1st Jan

Yang, X., Wang, Y., Yin, T., Wang, C., Lauret, N., Regaieg, O., ... & Gastellu-Etchegorry, J. P. (2022). Comprehensive LiDAR simulation with efficient physically-based DART-Lux model (I): Theory, novelty, and consistency validation. *Remote Sensing of Environment*, *272*, 112952.

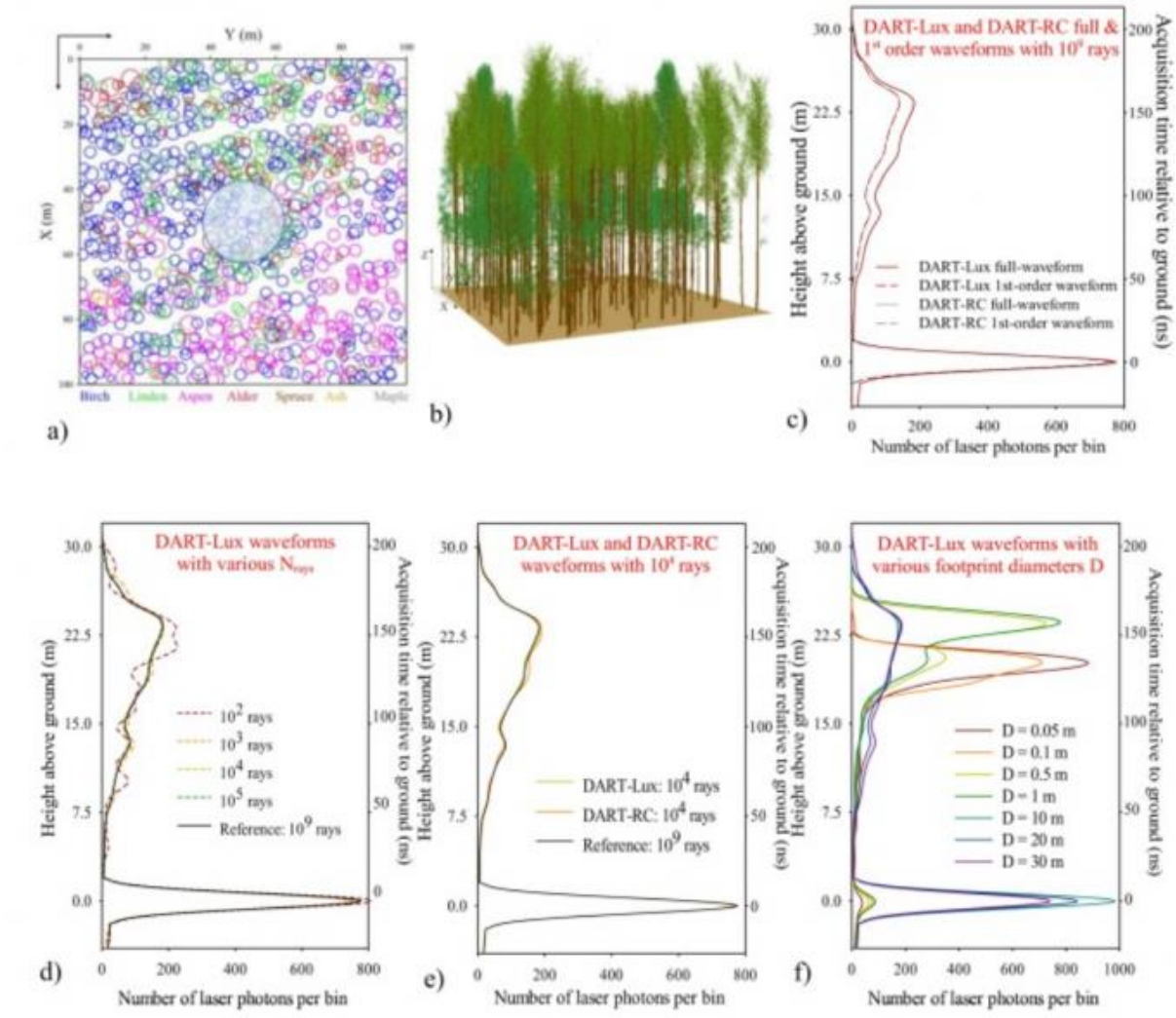

I could not fully digest this paper but I want to check the theory later. It would be great to check the vertical light information to understand under/over story physiology.